Dolomitization of Triassic microbial mat deposits (Hungary): Origin of microcrystalline dolomite

Kinga Hips[a*], János Haas[b], Zsófia Poros[a,c], Sándor Kele[d], Tamás Budai[e]

[a]MTA–ELTE Geological, Geophysical and Space Science Research Group, Pázmány s. 1/c, 1117 Budapest, Hungary (*Tel.: +36 1 3722500; fax: +36 1 3812128; e-mail: hips@caesar.elte.hu)
[b]Eötvös Loránd University, Pázmány s. 1/c, 1117 Budapest, Hungary
[c]currently: ConocoPhillips Company, 600 N Dairy Ashford, 77079, Houston, TX, USA
[d]Institute for Geological and Geochemical Research, Research Centre for Astronomy and Earth Sciences, Hungarian Academy of Sciences, Budaörsi u. 45, 1112 Budapest, Hungary
[e]University of Pécs, Ifjúság u. 6, 7624 Pécs, Hungary

Keywords: Microbial microfabric, Organogenic dolomite, Stable carbon and oxygen isotopes, Fluid inclusions

Abstract

Dolomite most commonly forms via replacement of precursor carbonate minerals. For this reason, diagnosing primarily precipitated organogenic dolomite in microbial mat deposits from the rock record is not straightforward, even though the deposits exhibit microbial fabric. Single and multiple dolomite crusts exhibiting microbial fabric occur in a pervasively dolomitized Middle Triassic platform succession. Two sections were studied in the Transdanubian Range. In both sections, two fabric types occur in the upper part of the metre-scale cycles. One of that is microbial boundstone (fabric type 1)—characterised by clusters of dolomite microcrystals which display diagnostic microbial features, such as calcimicrobes, clotted–spherular aggregates and globules. The other one is different in the two studied sections. In Section 1, it is micritic dolomite (fabric type 2) that is characterised by predominantly fine crystals and contains obscured microbial components. In Section 2, it is bioclastic dolomite (fabric type 3) that is rich in reworked dasycladalean alga fragments and consists of dolomite crystals of wide size-range from fine to coarse. The precipitation of the microcrystalline dolomite phase is interpreted as being facilitated by mats and biofilms favouring/tolerating an increasing frequency of subaerial conditions in the upper intertidal setting. Petrographic analyses revealed that organogenic calcite was also precipitated, especially

in mat deposits rich in bioclasts. Synsedimentary dolomitization, resulting in fine crystals, was coupled with aragonite dissolution and it postdated the organogenic precipitation. It took place only in the peritidal caps of the shallowing-upward depositional units. Petrographic analyses provide circumstantial evidence constraining that microcrystalline dolomite did not form via mimetic replacement. Accordingly the microcrystalline dolomite, which shows microbial microfabrics in the studied samples, is interpreted as an organogenic primary precipitate. Both peritidal processes, dolomite precipitation and replacement, were likely controlled by the environmental factors in a semi-arid climate. Those components of the platform succession that were not dolomitized in the peritidal environment were replaced and cemented by medium and coarsely crystalline dolomite during further burial at elevated temperature, as shown by fluid inclusion homogenisation temperature (62 to 83 °C) and negative stable oxygen isotope values. Thus, the majority of the studied formation consists of fabric-destructive dolomite (fabric type 4).

1. Introduction

Currently, one of the most challenging issues in the field of carbonate sedimentology and geochemistry is to understand the processes responsible for the mineralisation of a microbial mat. Studies in the last 30 years have elucidated the precipitation processes and suggested genetic models for microbially mediated dolomites (e.g. McKenzie, 1981; Baltzer et al., 1994; Vasconcelos et al., 1995; Wright 1999; Mazzullo 2000; van Lith et al., 2003; Bontognali et al., 2010). These studies emphasise that bacterial degradation of EPS organic matter is of major importance in the formations of microbial carbonates (e.g. Défarge et al., 1996; Decho et al., 2005; Braissant et al., 2007; Gallagher et al., 2012; Krause et al., 2012). Recently, Roberts et al. (2013) found a common association of dolomite precipitation with templates rich in certain organic matter, which are carboxyl-groups, whose high densities occur in degraded natural organic matter and in certain microbial surfaces.

Dolomite is a common diagenetic mineral in ancient carbonate rocks and reviews on its genesis are numerous (Land, 1985; Tucker and Wright, 1990; Budd, 1997; Warren, 2000; Machel, 2004; among others). It is generally recognised that dolomite forms via a dissolution–precipitation reaction in which a calcium carbonate precursor is replaced by calcium–magnesium carbonate through interaction with magnesium-rich fluids. Recently, studies in the Coorong lakes, Australia (Wright, 1999, 2000; Wright and Wacey, 2005) and in the coastal environments of the Persian Gulf, United Arab Emirates (Bontognali et al., 2010) suggested an organogenic precipitation model for that type of dolomite instead of the conventional models of replacive dolomite formation by evaporative seepage and/or hydraulic pumping. Diagnosing these genetic types, (1) organogenic dolomite or (2) organogenic calcium carbonate that was subsequently mimetically replaced by dolomite, in ancient microbial mat deposits, is extremely difficult.

Theoretically, a petrographic distinction between the two alternatives is not possible in the rock record because of the highly similar precipitation patterns of different carbonate minerals and resulting morphologies documented from recent microbial mat deposits (e.g. Monty, 1976; Dupraz et al., 2004; Bontognali et al., 2010; Couradeau et al., 2013). However, microbially mediated dolomite genesis was interpreted by recognising sub-micrometre-sized spheroids in a few papers on ancient Phanerozoic stromatolite, for example Mastandrea et al. (2006), Perri and Tucker (2007) and You et al. (2013).

Dolomites are characterised by a wide range in stable carbon isotope ratio. Mazzullo (2000) reported that dolomite crystals associated to sulphate reduction or methanogenesis typically are ^{13}C-depleted and ^{13}C-enriched, respectively. Many of the ancient shallow platform carbonates are evidently dolomitized in multiple phases. Although the dolomites of different genesis have distinct stable isotope signals, as a rule, the dolomite crystal phases—especially in the case of submicron-sized crystals—cannot be sampled and measured separately via routine analysis from ancient rock samples. Moreover, in the case of ancient rocks, it is not possible to determine whether disordered protodolomite or ordered dolomite precipitated primarily (cf. Wenk et al., 1993).

Petrographic analyses revealed that Middle Triassic shallow-marine carbonates of the Budaörs Dolomite contain peritidal deposits. Microfabrics indicate syndepositional organogenic carbonate precipitation in microbial mat deposits and synsedimentary dolomitization. The main objective of this study is to analyse the facies-relationship of the diagenetic components which reveals the spatial and temporal succession of diagenetic processes including organogenic precipitations and synsedimentary dolomitization.

Early stage synsedimentary dolomite occurs only in relatively thin intervals of the studied Middle Triassic carbonates. Subsequent diagenetic overprint by additional dolomitization and dolomite cement precipitation at intermediate burial depth is indicated by petrographic, geochemical and fluid inclusion data. These later processes resulted in pervasive dolomitization of a thick succession.

2. Geologic setting

The study area is located in north-central Hungary where the Triassic platform carbonates are exposed at the surface in the north-eastern part of the Transdanubian Range (in the Buda Hills and Zsámbék Basin; Figs. 1, 2). The present-day structural position of these rocks is the result of a large-scale displacement during the Tertiary (Csontos and Vörös, 2004). In the Middle Triassic, rift tectonics formed topographic highs with thick carbonate platform succession and coeval basins with limestone and tuff layers (Haas and Budai, 1995; Budai, 2004). Based on the relatively well-preserved dasycladalean algae (Kutassy, 1927; Piros unpublished data in Haas and Budai, 2004) the studied Budaörs Dolomite was assigned to the

Middle Triassic (uppermost Anisian–Ladinian) and was correlated with the South Alpine Schlern Formations 1–2 (Masetti and Neri, 1980; Rüffer and Zühlke, 1995; Haas and Budai, 1999). The thickness of the extensively dolomitized Middle Triassic platform carbonates is at least 1000–1200 m that was estimated through compiling the geological map. In spite of the relatively great thickness the formation is only discontinuously exposed. Based on a geological mapping of the region (Wein, 1977) two lithofacies were recognised. (1) Massive dolomite generally occurs in great thickness and occasionally contains dasycladalean algae. (2) Laminated dolomite contains cement-filled fenestral pores that define this lithofacies as stromatolite. The latter lithofacies is exposed only at some locations. Facies succession within the formation has not been studied yet.

Successively, in the course of the Late Triassic spreading stage, fault-controlled extensional basins were developed via segmentation of the Middle Triassic carbonate platform in a number of locations (Haas, 2002) whereas development of a shallow platform continued on vast areas (Main Dolomite/Hauptdolomit Formation). The rocks of the Buda Hills were subjected to moderate deformation during the Cretaceous. Thrust faults, folds and associated strong brecciation were observed in the studied dolomite (Fodor et al., 1994). Due to tectonically-induced uplifting and intense denudation in the Late Cretaceous and Early Neogene, post-Triassic Mesozoic formations are absent from the Buda Hills. Intensive tectonic activity in the Late Eocene led to block faulting and brecciation. The fractures formed due to the tectonic activity and the connected open pores of dolomite are filled with sediment consisting of silt-sized dolomite clasts, which was later silicified (Magyari, 1994). In the study area, eroded surfaces of dolomite are overlain by breccia and conglomerate that were formed in the surroundings of coastal cliffs via abrasion during the Late Eocene (Magyari, 1999). Calcite, barite, fluorite and associated sulphide minerals were precipitated along fractures within dolomite from hydrothermal basin-derived fluid expelled along Middle Miocene faults (Márton and Fodor, 2003; Győri et al., 2011; Poros et al., 2012). The inversion of the Neogene Pannonian Basin began in the latest Miocene and resulted in the uplift of certain basement blocks, among them the Mesozoic–Palaeogene block of the Buda Hills.

3. Materials and methods

Sampling of the Middle Triassic Budaörs Dolomite was concentrated on specific lithofacies; accordingly two short sections were studied where stromatolite and dasycladalean alga-rich lithofacies occur (Figs 1, 2). Section 1 is located at the cliffs north of Budaörs where two metre-scale intervals were sampled: three samples were taken from the lower 5.8 m (samples 1–3) and eight from the uppermost 2.1 m (samples 4–11). There is an approximately 8-m-thick covered interval between them. Section 2 is located in an

abandoned quarry west of Zsámbék from where four samples (12–15) were collected from a 1-m-thick interval.

Twenty-two thin sections were examined by conventional petrographic microscopy. The potential presence of organic matter was evaluated using a microscope equipped with an Hg vapour lamp and filters for blue light excitation (450–490 nm). The filter set was composed of a diachromatic beam splitter (510 nm) and a barrier filter (515 nm). Cathodoluminescence (CL) petrography was carried out using a Nuclide ELM–3R cold cathodoluminescence device operating at 10 kV. In order to distinguish between calcite, dolomite, and their ferroan variants, all the thin sections were stained with Alizarin Red-S and potassium ferricyanide as described by Dickson (1966).

Electron microprobe analyses (EPMA) were carried out for quantitative geochemical analysis of one selected, polished, carbon-coated sample (No. 10). The measurements were done by a JEOL JXA-8600 Superprobe (upgraded with SAMX control). The operational parameters and standards were the following: 15 kV acceleration voltage, 20 nA probe current, 5x4 μm defocused beam, PAP correction, dolomite USNM 10057 (for Ca and Mg), siderite USNM R 2460 (for Fe) and strontianite NMNH R 10065 (for Sr), and CO_2 was fixed to 46,90 wt. %. Distinct dolomite fabrics were sampled for stable carbon and oxygen isotope analyses, using a hand-held microdrill with a 0.5 mm bit-head. The carbonate powders were divided into two subsamples that were measured separately. The powders were analysed using the continuous flow technique with the H_3PO_4 digestion method (Rosenbaum and Sheppard 1986; Spötl and Vennemann, 2003). $^{13}C/^{12}C$ and $^{18}O/^{16}O$ ratios of CO_2 generated by acid reaction were measured using a Thermo Finnigan Delta Plus XP continuous flow mass spectrometer equipped with an automated GasBench II. The results are expressed in the δ-notation [$\delta = (R_1/R_2 - 1) \times 1000$] where R_1 is the $^{13}C/^{12}C$ or $^{18}O/^{16}O$ ratio in the sample and R_2 the corresponding ratio of the Vienna Pee Dee Belemnite (V-PDB) standard, in parts per thousand (‰). Duplicates of standards and samples were reproduced to better than ±0.15 and ±0.1‰, for oxygen and carbon isotopes, respectively.

For fluid inclusion studies, 80–100-μm-thick, doubly polished thin sections were prepared. In order to minimise sample heating and fluid inclusion stretching during sample preparation, a low-speed saw was used for cutting the rock samples. Conventional fluid inclusion petrography and microthermometry were performed on a Linkam FTIR 600 heating–cooling stage mounted on a polarisation microscope. Standardisation was carried out at temperatures of –56.6, 0 and 385 °C using quartz wafers containing synthetic H_2O and H_2O–CO_2 fluid inclusions. The accuracy of the measurements during freezing experiments and heating up to 150°C was 0.1°C.

4. Petrography

The studied pervasively dolomitized successions consist of two alternating lithofacies occurring in metre-scale cyclic packages. The light grey massive lithofacies is overlain by a white thin-bedded/laminated one (Fig. 2). Their transition is gradual. Both lithofacies could be subdivided into more fabric types by microscopic study. Accordingly, all together four fabric types are distinguished, which occur systematically in accordance with the depositional succession (from bottom to top): fabric-destructive dolomite and bioclastic dolomite are found in massive lithofacies whereas micritic dolomite and microbial boundstone characterise the thin-bedded/laminated one. Dolomite veinlets cut across both lithofacies and detrital dolomite occurs as internal sediment in pores and fractures.

Altogether four non-ferroan dolomite crystal phases (DOL-1–4) were identified and classified according to the crystal-size and textural relationships. These are as follows; DOL-1 is microcrystalline dolomite which is defined by submicron-sized crystals; DOL-2 is finely crystalline replacive dolomite which is typified by micrite and microspar-sized crystals; DOL-3 is medium and coarsely crystalline replacive dolomite which is characterised mostly by 70–350-μm-sized turbid crystals; and DOL-4 is dolomite cement which forms a limpid overgrowth zone on DOL-3 phase maximum at a thickness of 150 μm.

4.1. Thin-bedded/laminated lithofacies

In Section 1, thin-bedded/laminated lithofacies is characterised by regular repetitions of thin layer-couplets consisting of micritic dolomite in the lower part and microbial boundstone above (Fig. 3). In Section 2, only thin microbial boundstone layers were observed. In micritic dolomite layers, characteristic components are the flat-pebbles at the base, ripped up from the underlying lithified layer. The size of reworked and rounded lithoclasts decreases upward and they disappear at the upper part of the layer. A dispersed brownish-colouring around the rip-up clasts is common. Burrow-mottled fabric is typical. Occluded laminoid fenestral pores occur more frequently in the microbial boundstone layer. The upper surface of microbial boundstone is often sharp, uneven and occasionally brecciated. Only a few skeletal fragments were encountered, mainly articulated and disarticulated ostracod valves, subordinately dasycladalean algae, foraminifera and gastropods.

4.1.1. Microbial boundstone, fabric type 1 (FT1)

Microbial boundstone fabric type is characterised by the ubiquitous presence of microcrystalline dolomite (DOL-1). These dense submicron-sized crystals form clotted–spherular aggregates and bundles of prostrate threads. The textural relationship of solid clots and chambered spheroids exhibits a size-related hierarchy such as aggregates of tiny clots gradually developing into aggregates of larger spheroids. Along

with an increasing size of the spheroids their inner part is less densely filled with microcrystals (Fig. 4). One of the most common microfabric types, where attached clots and associated hollow spheroids form closely packed, upward-expanding bushy aggregates, resembles *Renalcis* and *Angusticellularia* calcimicrobes (Pratt, 1984; Riding, 2000; Stephens and Sumner, 2002). Additionally, tufted filamentous calcimicrobes, which resemble *Cayeuxia* (Riding, 1991), are occasionally preserved and surrounded by clotted aggregates. Uniform, oval-shaped globules of *ca* 10–20-μm-size are closely packed and embedded in dense microcrystalline groundmass (Fig. 4).

Finely crystalline dolomite (DOL-2) is characterised by micrite and microspar-sized crystals and is present in certain intervals where their amount decreases upward. The mixture of microcrystalline aggregates and fine crystals occurs as a massive groundmass or forming a nodular and/or reticulate microfabric (Fig. 5A, B). The DOL-1 shows bright green fluorescence whereas a mixture of DOL-1 and DOL-2 exhibits dull green fluorescence under blue light (Fig. 5C). Both dolomite types display dull red luminescence under CL but the luminescence of the mixture of DOL-1 and DOL-2 is less intense (Fig. 6).

The microstructure of FT1 is typified by cyclic packages of lamina-couplets, which consist of lower nodular/reticulate lamina and overlying dense–clotted microcrystalline lamina (Fig. 5A).

4.1.2. Micritic dolomite, fabric type 2 (FT2)

Micritic dolomite is characterised by the abundance of fine crystals of mostly micrite-size (up to *ca* 20 μm; DOL-2). The fabric additionally includes faint microcrystalline clot clusters (DOL-1) and medium-sized subhedral crystals (DOL-3) in a heterogeneous mixture with fine crystals (Fig. 7). In the upper part of the layer, poorly-defined calcimicrobes (DOL-1) are definitely present and become well-defined and abundant in the overlying microbial boundstone. Under blue light, this fabric exhibits a heterogeneous dull green and non-fluorescent groundmass with dispersed brighter clots and spots (Fig. 7B, D).

In the lower part of Section 1, the thin-bedded/laminated lithofacies are the thinnest. Here the upper surface of the micritic dolomite layers is commonly uneven, brecciated and the microbial boundstone (FT1) is absent. Upsection the microbial microfabric progressively becomes obvious through the increasing abundance of DOL-1 crystals among the DOL-2 micrite crystals but FT1 is commonly very thin. In the upper part of Section 1, at microscopic scale, the upward transition from micritic dolomite to microbial boundstone is manifested either in lamina-scale alternations or in a patchy microstructure. In the latter case, the nodular microfabric type (FT1) forms irregular and discontinuous patches within the micritic dolomite (FT2).

4.1.3. Pore types and infilling phases

Open porosity is absent or very minor in the studied samples, but several different occluded pore types were observed. Arborescent clumps are ubiquitous in the microbial boundstone (FT1) and among them occluded pores of a wide size-range occur. The pores formed a complex network system that was occluded by internal sediment and cement infillings (Figs 4, 5). The volume of the original pore space was significant and thus, pores were major components of the microfabric. Three pore types can be distinguished. The most common type included fenestral and/or desiccation pores of variable sizes and shapes, from some tens of micrometres up to several millimetres. The relatively large pores were typically, but not exclusively, elongate and sub-parallel to the bedding. The second type of original pores was a biomould, and the third includes thin fractures and breccia pores.

In certain intervals in Section 2, two dolomite phases occluded the fenestral/desiccation pores, which are fine crystals in micrite size (DOL-2) and brownish anhedral crystals in medium size (*ca* up to 130 μm; DOL-3). The DOL-3 phase appears as sets of elongate crystals. They exhibit sweeping extinction that moves into one direction. Fine crystals (DOL-2) densely or dispersedly surround the brownish crystals in a heterogeneous pattern. These DOL-2 and DOL-3 crystals are mostly non-fluorescent but exhibit faint green mottles (Fig. 4C, D). Locally, brownish-coloured pendant linings are observed at the roof of larger pores where fine crystals show dull green fluorescence in bands (Fig. 4C, D).

Variable amounts of fine crystal silt (DOL-2) cover the bottom of voids in microbial boundstone both in Section 1 and 2. The dolomite silt contains lithoclasts originated from the roof of the cavity. In certain beds, a larger amount of dolomite silt completely occluded most of the pores or formed cap-lamina containing floating tattered microbial boundstone fragments. Under blue light, the crystal silt exhibits dull green fluorescence (Fig. 5). Fractures cut across all the above described components.

The rest of the pore space in microbial boundstone was occluded by two generations of dolomite crystals, DOL-3 and DOL-4 (Fig. 5). The first phase (DOL-3) is characterised by blocky crystals that are slightly turbid because of the inclusions (Figs 5B, 6C). Many of the solid inclusions are brownish in colour. The crystals show mottled fluorescence and luminescence, i.e. scattered, bright spots appear in a non-fluorescent/non-luminescent background (Figs 5C, 6D). Except for the largest pores, the first generation crystals generally occlude the entire pore space. Where it does not, the second generation of crystals (DOL-4) appears as limpid optical overgrowth on the DOL-3 phase that is typified by rhombohedral termination (Fig. 5B). These crystals have straight or very faint undulose extinction. Two growth bands in the DOL-4 cement phase are visible under blue light as well as under CL. The first one exhibits dull fluorescence with fine subzones and is non-luminescent whereas the second one shows the opposite pattern, being non-fluorescent and of dull luminescence with fine subzones (Figs 5B–C, 6C–D).

In micritic dolomite (FT2), limpid subhedral crystals fill a pore network system that is more obvious in the upper part of the layers (Fig. 7C). The crystal size is *ca* 70–90 μm in the lower part of the layers and

gradually increases upsection up to 250 μm (DOL-3 and DOL-4). These crystals show growth bands under blue light that are similar to the pattern of the two generations of pore-filling crystals in the FT1 (Fig. 7).

Fractures cut across the above-described components, which are filled with silicified internal sediment consisting of silt-sized dolomite (Fig. 3). Silicified dolomite silt is the last pore-occluding phase, post-dating the DOL-4 dolomite cement phase, in the largest, bedding-parallel pores (Fig. 5B, C). The internal sediment often includes detrital fragments of the DOL-4 cement crystals.

4.2. Massive lithofacies

Massive lithofacies is characterised by a lack of any macroscopic sedimentary structure and it includes bioclastic dolomite and fabric-destructive dolomite. In Section 1, sets of lamina-couplets, identical to those observed in the thin-bedded/laminated lithofacies (FT1–FT2), are present but they are only detectable in thin sections. Bioclastic dolomite occurs only in Section 2 where it overlays fabric-destructive dolomite. Dasycladalean alga fragments are abundant in the bioclastic dolomite; in addition, foraminifers, gastropods and crinoid ossicles are also present, scarcely. Lithoclasts of microcrystalline dolomite are locally very common in both fabric types, especially in those samples, where this lithofacies overlays microbial boundstone.

4.2.1. Bioclastic dolomite, fabric type 3 (FT3)

Although the bioclastic dolomite can be classified as fabric-destructive dolomite the depositional texture is partly reflected by the variable crystal size as well as the brownish-staining (due to the abundance of solid inclusions) of the coarser crystals (Fig. 8A). Bioclastic dolomite is characterised by medium and coarsely crystalline dolomite consisting of closely packed subhedral–anhedral crystals up to *ca* 400 μm in size (DOL-3 and DOL-4). These crystals show undulose extinction under crossed polars. Additionally, finely crystalline dolomite (DOL-2), consisting of micrite-sized crystals, appears at the bottom of various pores and otherwise heterogeneously dispersed in the fabric. The DOL-3 phase exhibits a distinct appearance and it is present in three forms, such as dark brownish mosaics, lighter brownish, isopachous elongate crystals and turbid mosaics. The dark brownish mosaic crystals are distributed in irregular patches and they cover the bioclasts. Elongate crystals occur in certain patches—among the ghosts of bioclasts and in the primary intraparticle pores of skeletal fragments—in the lower part of FT3 intervals (Fig. 8B). The sets of elongate crystals exhibit sweeping extinction, which moves into one direction. The various crystal phases display distinct fluorescence under blue light (Fig. 8C, D).

The bioclastic dolomite shows gradual transition to microbial boundstone (FT1). In the transitional interval, microcrystalline clot clusters (DOL-1) occur together with dark brownish-stained, fine to

medium-sized anhedral mosaic crystals (DOL-3; Fig. 9). The amounts of both the brownish mosaic crystals and the bioclasts decrease upward; thereafter, they became subordinate or disappear in the overlying microbial boundstone along with the increasing amounts of clot clusters of DOL-1 microcrystals.

4.2.2. Fabric-destructive dolomite, fabric type 4 (FT4)

Fabric-destructive dolomite is predominantly characterised by a medium crystalline (70–250 μm) dolomite consisting of closely packed subhedral–anhedral crystals (Fig. 10). Locally, fine and coarser crystals may also co-occur (*ca* up to 350 μm). The crystals are variably inclusion-rich, or characterised by turbid core and limpid rim (DOL-3 and DOL-4, respectively). The majority of crystals show undulose extinction. Under blue light, the limpid crystals exhibit a fluorescence pattern that is highly similar to that of the pore-filling cement phase (DOL-4) within FT1; otherwise, this fabric typically shows blotchy fluorescence.

In the lower part of Section 1, the fabric-destructive dolomite shows a gradual transition upsection to the lamina of the microbial boundstone that was observed in thin sections. At the lower part of the transitional interval, DOL-2 fine crystals appear and they become more common upwards. Under blue light, the fabric-destructive dolomite exhibits a spongy fabric that is very similar to the fabric of the overlying microbial boundstone, but along with an increasing crystal size the fabric progressively becomes obscured (Fig. 10B, C).

5. Geochemical data

5.1. Major and trace element compositions

Although the back-scattered electron image of dolomite crystals displayed grey-scale heterogeneity there are no measurable differences in chemical compositions between contrasting areas of any of the dolomite types. Concentrations of trace elements were below the detection limit of the EPMA.

5.2. Stable carbon and oxygen isotopes

The heterogeneity of the dolomite crystals inhibited their separate sampling. The DOL-3 and DOL-4 crystal phases were sampled and measured together from the largest pores. In all other samples, bulk rock powders containing multiple dolomite crystals were analysed (Table 1; Fig. 11). The $\delta^{13}C_{V\text{-}PDB}$ values of all analyses are similar, ranging between 2.2‰ and 3.9‰. In contrast, the $\delta^{18}O_{V\text{-}PDB}$ values of DOL-3 and

DOL-4 phases from large pores (–4.3‰ to –1.7‰) are depleted in ^{18}O relative to those of bulk samples. Bulk samples from microbial boundstone, micritic dolomite and bioclastic dolomite (potential mixtures of all types of dolomite crystals) yielded $\delta^{18}O_{V\text{-}PDB}$ values of 0.2‰ to 1.2‰. The fabric-destructive dolomite has values in a wide range. The sample (No. 3; Table 1) containing predominantly DOL-3 crystals has values –1.9 and –0.1‰. The other sample (No. 10; Fig. 10A) containing lithoclasts has a value 0.3‰. The sample (No. 1; Fig. 10B, C), which contains a microcrystalline microbial boundstone lamina in thin-section-scale and a relatively large amount of fine crystals among the medium-sized crystals, has a value of 1.6‰ at 1 cm below the nodular part of the lamina, and 0.7‰ and 1.1‰ at 2 cm and 3 cm below that one, respectively.

6. Fluid inclusion petrography and microthermometry

In order to obtain information on the temperature and the composition of dolomitizing fluid(s), fluid inclusions of two samples from microbial boundstone layers (Section 1) were studied in detail (Table 2; Fig. 12). Fluid inclusion data from fabric-destructive dolomite samples of the same formation from a nearby outcrop were also available (Poros, 2011). In one of the microbial boundstone samples, only the pore-filling DOL-3 and DOL-4 crystals contained measureable aqueous fluid inclusions. In the other sample, measurable fluid inclusions were found also in the fabric-destructive dolomite that occurs in centimetre-scale patches at the crossing of dolomite veinlets in the upper part of the microbial boundstone layer.

In the pore-filling crystals, the appearance of fluid inclusions in the turbid DOL-3 generation and the limpid DOL-4 is identical; however, the abundance of inclusions in the limpid rim is significantly lower compared to the other phase. Most of the primary aqueous inclusions contained both liquid (L) and vapour (V) phases (Fig. 12A). In the turbid crystals, the primary inclusions were found along growth zones, whereas primary inclusions of the limpid rim are randomly distributed. At room temperature, the vapour bubble was moving in the case of most inclusions. All-liquid inclusions were also rarely observed; however, where seen they were close to two-phase inclusions, presenting evidence for necking-down after phase separation. Those two-phase inclusions, located next to single-phase ones, were not measured. The size of the measured inclusions ranges between 5 and 15 μm. The visually-determined liquid–vapour ratio ranges between 95:5 and 90:10; and no gas-rich inclusions occur.

Euhedral crystals of the fabric-destructive dolomite sample contain similar fluid inclusions to the previous sample. However, in this sample, not only the euhedral crystals but also the replacive finer, anhedral and subhedral crystals (DOL-3) contain small (*ca* 3 μm), but still measurable, randomly distributed two-phase (L–V), aqueous fluid inclusions.

373 All the measured DOL-3 and DOL-4 crystal phases exhibited similar ranges in homogenisation
374 temperatures (Th) of the primary two-phase inclusions. Homogenisation temperature in turbid DOL-3 and
375 limpid DOL-4 crystals ranged between 72 and 79 °C, with one outlying value at 90 °C which is
376 considered to be invalid due to the supposed volume change after entrapment. Anhedral and subhedral
377 DOL-3 finer crystals of the latter sample show a slightly wider and lower temperature range from 62 up to
378 83 °C (Fig. 12B). 90% of all the data from the different crystals fall into a narrow range from 73 to 83°C.
379 Entrapment temperatures of the fluid could not be calculated (i.e. no pressure correction was applied), but
380 the homogenisation temperature values still provide a valid measure of the minimum entrapment
381 temperature (Goldstein and Reynolds, 1994).
382 Cryoscopic and heating measurements could not be carried out on the same inclusion, because the
383 vapour bubble disappeared during homogenisation and never reappeared. Cryoscopic measurements were
384 not successful on other inclusions because the vapour phase became metastable during freezing, probably
385 because of the very low vapour/liquid ratio. It was also not possible to detect the eutectic temperature
386 because of the very small size of the inclusions. Only, three inclusions were appropriate for salinity
387 measurements. All of them were hosted by the turbid core of the dolomite crystals (DOL-3). The salinity
388 values calculated from the final melting temperatures, assuming a NaCl–H_2O system, are 3.4, 3.8, and 6.4
389 NaCl equ. wt. %.
390
391 **7. Discussion**
392
393 *7.1. Interpretation of sedimentary features*
394
395 *7.1.1. Microbial boundstone (FT1)*
396 The ubiquitous presence of microcrystalline dolomite (DOL-1) in the form of dense groundmass, clots,
397 clot clusters and calcimicrobes suggests that the FT1 was derived from the mineralisation of bacterial EPS
398 (Riding, 2000). Observations on modern and recent benthic microbial mat communities indicate that
399 micrite nucleation is initiated within the EPS and its alveolar organic network is progressively replaced by
400 mineral precipitation, high-Mg calcite (e.g. Défarge et al., 1996; Gautret et al., 2004; Dupraz et al., 2004),
401 aragonite (e.g. Monty, 1976; Couradeau et al., 2013), or dolomite (e.g. Bontognali et al., 2010).
402 Accordingly, a wide variety of precipitation patterns may be developed, which is reflected by the
403 microfabric. These patterns include dispersed smaller and larger spheroids (Bontognali et al., 2010),
404 spherular aggregates (Wright, 1999), clots and clot clusters progressing into a massively mineralised
405 groundmass (Dupraz et al., 2004), dissected or continuous laminae (Visscher et al., 2000) and
406 calcimicrobes (e.g. Riding, 2000).

In the studied samples, the microfabric components are consistent with carbonate mineral precipitate morphologies that have been recorded from modern EPS substrate. The spongy fabric is due to the fenestral pores, formed penecontemporaneously within the EPS during the degradation of organic matter (Défarge et al., 1996) and desiccation pores, formed successively during ephemeral subaerial exposure (Shinn, 1983). Additionally, tiny globules accompany the most abundant microcrystalline precipitates. Their size and shape resemble empty ghost remnants of coccoid cyanobacterial sheaths (cf. Dupraz et al., 2004; Golubic and Abed, 2010). The fluorescence in the microcrystalline components is most likely caused by the associated diffuse organic matter (e.g. Dravies and Yurewicz, 1985; Bertrand et al., 1986). Coexistence of carbonate mineral precipitation and organic matter requires anoxic and slightly alkaline conditions (Krumbein and Garrels, 1952; Visscher and Stolz, 2005), and under such conditions, Mn^{2+} could build in the carbonate lattice and that Mn^{2+} even in small amounts could have activated the fluorescence (Gaft et al., 2005). Fine detrital sediment (replaced by DOL-2) was incorporated into the mat and amalgamated with microcrystalline aggregates, forming reticulate or nodular microfabrics in the course of diagenesis. However, an alternative, such as microcrystalline aggregates merging through further precipitation (cf. Dupraz et al., 2004; Bontognali et al., 2010; Spadafora et al., 2012), cannot be excluded.

7.1.2. Micritic dolomite (FT2)

Obscured microbial components indicate that the buried microbial mat was definitively present in the precursor of the micritic dolomite but its preservation was limited. The downward decreasing size of the antecedent pores (later filled by cement crystals) is attributed to physical compaction, also implying diffuse mineralisation of the mat (cf. Dupraz et al., 2009). The abundance of sand-sized detrital sedimentary grains, together with the bioturbational mottles, suggests that detrital micrite was also present as sedimentary components. The detrital carbonate mud was replaced by the fine dolomite crystals (DOL-2).

7.1.3. Bioclastic dolomite (FT3)

The bioclasts are embedded within patches of dark brownish-stained DOL-3 mosaic crystals that are interpreted, on the basis of the clotted fluorescence pattern, as replaced organogenic precipitate. The spongy pore network within the precursor, filled by DOL-2–4 phases, is interpreted as having a fenestral/desiccation origin. This also implies the predominance of microbial precipitation within this fabric type. Accordingly, the precursor deposits of the bioclastic dolomite were determined by a microbial mat. The mineral phase of the organogenic precipitate (precursor of brownish-stained DOL-3 mosaic crystals exhibiting bright green fluorescence) is interpreted as having been high-Mg calcite (HMC) since

this is typical in a marine setting (Dupraz et al., 2009). Aragonite is excluded since aragonite bioclasts were not dolomitized in this fabric type; they were selectively dissolved leaving mouldic porosity (Figs 8, 9). A microcrystalline precursor is assumed because this is the documented size of crystals forming clotted fabric (Riding, 2000; Dupraz et al., 2009). The meteoric diagenetic origin of the observed features is not supported by the measured oxygen isotope data (discussed below in the paragenetic sequence).

7.1.4. Fabric-destructive dolomite (FT4)

The medium crystalline dolomite marks pervasive alteration since no original sedimentary texture has been preserved, except for the reworked lithoclasts. Dolomitization resulted in medium crystals and obliterated all features of the precursors, which is clearly reflected in the fluorescence properties. The turbid crystals or cores of individual crystals (DOL-3), which likely preserve solid relics of the precursor carbonate, were altered via replacement (Land et al., 1975). The overgrowth limpid rim and limpid crystals exhibit similar fluorescence to that of the DOL-4 cement generation within the microbial boundstone; thus, they were also precipitated as cement (Choquette and Hiatt, 2008). Spongy network revealed by the fluorescence pattern in the transitional interval toward the microbial boundstone (Fig. 10B, C) suggests a microbial deposit precursor including organogenic precipitates. Similarly to the bioclastic dolomite the organogenic mineral phase, which was replaced partly by DOL-2 fine crystals and partly by DOL-3 medium-sized crystals, is interpreted as having been HMC.

7.2. Depositional environment of microbial mats and biofilm

In the studied samples, the observations imply the following constraints on microbial deposits. A decreasing energy of tidal current across the tidal flat is reflected in the composition and size of trapped sedimentary particles. The overall presence of reworked bioclasts in microbial mat deposits (bioclastic dolomite, FT3) indicates permanent connection to a normal marine subtidal zone. The coarser sediment influx was likely controlled by storms and provides evidence for a higher-energy setting and more frequent inundation. Fine dolomite crystals (DOL-2) in the microbial mat deposits appear to have originated from dolomitized fine marine sediment and partly likely from trapped aeolian dolomite silt. The latter could have been transported from the exposed supratidal zone (e.g. Shinn, 1983). Fine sediment was supplied by tidal currents to the lower intertidal zone (micritic dolomite, FT2 and bioclastic dolomite, FT3) but the mat was less frequently inundated in the upper intertidal zone (microbial boundstone, FT1), which is reflected by the upward decreasing amount of fine crystals. In the supratidal zone, a thin layer of dolomite silt covered the mat surface.

The reticulate/nodular laminae (FT1, lower part) resemble the features of a pustular mat, such as the way in which the interior heterogeneity reflects the irregularity of the surface by high porosity and internal sediment infilling (Monty, 1976; Halley, 1976). This mat type is mostly reported from the hypersaline upper intertidal zone (e.g. Allen et al., 2009; Abed et al., 2010). Smooth laminae of dense microcrystals with abundant globules (FT1, upper part) likely record the uppermost intertidal thin biofilm composed predominantly of coccoid cyanobacteria (e.g. Jahnert and Collins, 2013). Therefore, the presence of microcrystalline dolomite (DOL-1) appears not only to be related to periods of ephemeral subaerial exposure but facilitated by a mat and biofilm favouring/tolerating an increasing frequency of mesohaline/hypersaline conditions.

7.3. Paragenetic sequence

7.3.1. Relative timing of dolomitization processes

The basic question is whether the wide variety of dolomite in the studied samples was created either by a single dolomitization process and thus, the formation of the distinct dolomite types was controlled by the heterogeneity in the precursor deposits, or by successive processes in various diagenetic environments. The combination of the succession of diagenetic events observed, the isotopic data and the fluid inclusion data indicates two stages of dolomitization (Fig. 13). The measured 62–83 °C homogenisation temperature on DOL-3 and DOL-4 implies their intermediate burial origin (Morrow, 1990; Machel, 2004). Burial dolomite can be expected to have negative $\delta^{18}O$ values due to precipitation at higher temperature at greater burial depth (e.g. Machel, 2004). The $\delta^{18}O$ values of the pore-filling DOL-3 and DOL-4 phases (between –4.3‰ and –1.7‰) correspond to the reported values of burial dolomite (e.g. Warren 2000). The bulk rock $\delta^{18}O$ values of the microbial boundstone, micritic dolomite and bioclastic dolomite (from 0.2‰ to 1.2‰) represent a rather distinct population. The difference between these two groups implies dolomitization by various fluids of different compositions rather than by the same fluid at a different temperature. Moreover, the first-stage dolomite crystal-association (DOL-1 and DOL-2) must be more enriched in heavier isotopes than the solid phase mixture since the latter (=bulk rock of FT1, FT2 and FT3) includes the DOL-3 and DOL-4 phases, too (cf. Banner and Hanson 1990). The estimated range of DOL-1 and DOL-2 together is approximately consistent with precipitates occurring under synsedimentary mesohaline condition (Land, 1983; Simms 1984). The completely fabric-destructive dolomite (FT4; with DOL-3 and DOL-4) is of relatively negative value (–1.9‰)—that is comparable with values of pore-filling DOL-3 and DOL-4 phases—which implies that the precursor was not affected by synsedimentary dolomitization. The presence of reworked microcrystalline to finely crystalline lithoclasts (DOL-1 and DOL-2 phases) and some fine DOL-2 replacive crystals within FT4 shifted the bulk rock isotope values (–0.1 and 0.3‰) that

also suggests two different dolomitization processes regarding the lithoclasts and the host deposits. The more positive values (0.7‰ to 1.6‰) are due to the common presence of replacive DOL-2 crystals within the transitional interval of FT4 below the microbial boundstone lamina (Fig. 10B, C). The measured $\delta^{13}C$ values point to seawater-derived pore-fluids.

Mineralisation of microbial biofilms by dolomite (DOL-1) and dolomitization of the associated sediments (DOL-2) were early synsedimentary diagenetic processes (Fig. 14). This is constrained by reworked detrital fragments of lithified microbial boundstone which occur in the overlying deposits represented by bioclastic and fabric-destructive dolomites. The internal sediment, encountered in mat deposits, was composed of dolomite silt and/or micrite sediment replaced by fine crystals (DOL-2). All these observations suggest that synsedimentary dolomitization occurred only in the peritidal caps of shallowing-upward cycles; otherwise, the majority of the deposit consisted of $CaCO_3$ before it was buried (Fig. 14).

7.3.2. Synsedimentary and near-surface processes

The sweeping extinction of elongate crystals (DOL-3 in FT1 and FT3) suggests that their precursor precipitated as a radiaxial fibrous calcite cement (RFC; *sensu* Kendall, 1985). Pendant and fibrous calcite (RFC) precipitated from a marine pore fluid (Frank and Lohmann, 1996) as a first phase cement that was observed in certain intervals of microbial boundstone and bioclastic dolomite in Section 2. Dolomitization of the RFC crystals resulted in fine (DOL-2) and coarser (DOL-3) crystals (Fig. 8B, C D). Fine dolomite (DOL-2), replacing partly the RFC crystals, suggests that dolomitization post-dated the cement precipitation. The dissolution of aragonite bioclasts post-dated the precipitation of RFC but predated the dolomite silt infilling (DOL-2). Thus, synsedimentary dolomitization (DOL-2) and the selective dissolution of aragonite took place penecontemporaneously.

The internal sediment, that infiltrated into the mouldic pores left behind after selective dissolution of aragonite, indicates that synsedimentary alteration of the deposits took place while the host sediment was in its original depositional setting. The alteration of sediments by selective/non-selective dissolution, cementation and mineral stabilisation via microspar replacement in a meteoric diagenetic environment is a characteristic feature in many cyclic shallow platform carbonates (e.g. Read and Horbury, 1993). In the studied samples, these features are not considered as indicators of intermittent diagenesis in freshwater because of the lack of remnants of calcrete components (such as joint occurrence of hairline circumgranular cracks and pendant cement, glaebules with composite inner fabric and pisoids) and the lack of inherited negative carbon isotope value. Theoretically fabric heterogeneity resulting from synsedimentary meteoric alterations might have been preserved during later-stage mimetic dolomitization

541 but the measured oxygen isotope values from the studied samples do not support single dolomitization
542 event.
543
544 *7.3.3. Shallow-burial and intermediate-burial processes*
545 Fluid inclusion microthermometry analyses yielded the similar homogenisation temperature ranges for
546 DOL-3 and DOL-4 crystals. In microbial boundstone, where they are pore-filling phases, the DOL-4
547 phase shows fluorescence zonation and makes up the optical overgrowth on the DOL-3 phase, which
548 shows mottled luminescence. On the bases of crystal habits, the DOL-4 was interpreted as having been
549 precipitated as cement after the DOL-3 replacement of the precursor calcite cement (CAL). The inherited
550 blocky crystal form of the DOL-3 suggests a blocky calcite precursor. Brownish, solid inclusions, which
551 show bright green fluorescence, are exclusively present in the CAL/DOL-3 replaced cement generation.
552 Petrographic characteristics suggest that these inclusions consist of organic matter. Remnants of organic
553 matter were likely dispersed within or among the precursor cement crystals and were preserved during the
554 replacement process. Considering the cyclic depositional setting the ubiquitous pore-filling cement phase
555 is thought to have been precipitated from marine-derived pore-water as calcite (CAL), post-dating the
556 synsedimentary replacive dolomitization (DOL-2), when peritidal mat deposits were submerged during
557 subsequent sea-level cycles. DOL-3 subsequently replaced any remnants of calcium carbonate, which
558 include calcareous deposit and calcite cement (remnants of RFC and CAL). The latest stage of
559 dolomitization was dolomite cement precipitation (DOL-4).
560 An intermediate burial dolomitization (summary in Machel, 2004), with seawater-derived fluids
561 circulated by thermal convection, would have had the capacity to drive DOL-3 and DOL-4 formation.
562 Numerical modelling of open half-cell thermal convection shows that convection can drive dolomitization,
563 mostly at temperatures greater than 50 °C and over time scales of millions to a few tens of millions of
564 years (Wilson et al., 2001; Whitaker et al., 2004; Whitaker and Xiao, 2010). Fluid supply was crucial in an
565 open circulation setting where the half-cell discharged toward the top of the thick, porous platform
566 carbonate, which does not contain any aquitards. Seawater is Mg^{2+}-rich and supersaturated with respect to
567 dolomite; thus it is an obvious source for dolomitization (e.g. Purser et al., 1994). However, this model
568 alone cannot explain the origin of a slightly hypersaline pore-fluid. Accordingly, it is presumed that an
569 exotic fluid was channelled through a deeply penetrating, low-angle master fault activated in an
570 extensional tectonic setting (cf. Doglioni, 1992; Bertotti et al., 1993) and injected into the fluid of
571 convection cells.
572
573 *7.4. Discussion on synsedimentary dolomitization: organogenic microcrystals and replacive fine crystals*
574

Petrographic comparison of the two dolomite fabric types, which exhibit microbial microfabric, suggests circumstantial evidence constraining that microcrystalline dolomite (DOL-1) did not form via a mimetic replacement process. Microbial boundstone (FT1) includes both synsedimentary dolomite phases, such as microcrystalline and finely crystalline ones, whereas bioclastic dolomite (FT3) does not involve the microcrystalline phase. In the latter case, the organogenic calcite precursor (HMC) was partly replaced by DOL-2 fine crystals in a peritidal environment and partly by brownish-stained DOL-3 medium-sized mosaic crystals during further burial. The DOL-3 crystals display bright fluorescence and reveal a clotted microbial fabric under blue light. Consequently, in a fabric where the DOL-1 microcrystals are present, this phase precipitated primarily (either in the form of protodolomite or as ordered dolomite; cf. Wenk et al., 1993). Moreover, replacement of organogenic HMC by DOL-2 in micritic dolomite (FT2) and in the transitional interval of fabric-destructive dolomite (FT4; Fig. 10B, C), where spongy fabric occurs, is also very probable. This interpretation is supported by the oxygen isotope data from the transitional interval of fabric-destructive dolomite showing a spongy pattern, where DOL-2 fine crystals co-occur with DOL-3 medium-sized crystals (sample 1; Table 1).

In the studied sections, the presence of the microcrystalline dolomite is facies-dependent. It appears and becomes abundant upwards within the thin layer-couplets where the fabric exhibits gradual transition either from micritic dolomite (FT2) to microbial boundstone (FT1) or from bioclastic dolomite (FT3) to microbial boundstone (FT1). According to the proposed model (Fig. 14), in the first step, organogenic high-Mg calcite was precipitated in the lower intertidal mat deposits whereas organogenic dolomite progressively took over its place in the buried upper intertidal mat and biofilm in the course of increasing frequency of subaerial exposure and under mesosaline conditions. In the transitional phase, dolomite co-precipitated together with high-Mg calcite. The microcrystallinity of primarily precipitated dolomite indicates rapid and multi-site nucleation on EPS organic substrate (cf. Kandianis et al., 2007; Krause et al., 2012). The results of Roberts et al. (2013) revealed that natural surfaces, including organic matter and microbial biomass, having a high density of carboxyl groups promoted the formation of ordered dolomite nuclei. Under a semi-arid climate, environmental conditions commonly show extreme annual variability in the salinity of the water and the extent of water coverage. Facies reconstruction of the studied formation revealed that the environmental factors likely controlled both the spatial distribution of microbial communities (cf. Yannarell et al., 2006; Paerl and Yannarell, 2010) and the precipitated minerals.

In cyclic peritidal succession, as a rule, the synsedimentary dolomitization correlates with prolonged periods of subaerial exposure during regressions (e.g. Mutti and Simo, 1994). The sabkha model of replacive dolomite formation (examples in Purser et al., 1994; Budd, 1997; Warren, 2000) cannot be applied to the studied formation because no traces of associated evaporite minerals were found. Under prolonged subaerial conditions, the shifting of the saturation state of the pore-fluid with respect to

609 aragonite and HMC is interpreted to have led to replacive dolomite formation. The reaction rate of organic
610 matter degradation controls the carbonate precipitation and dissolution by influencing the pH (Ben-
611 Yaakov, 1973). For example high rates of bacterial sulphate reduction near the surface coincide with
612 microcrystalline carbonate precipitation (Visscher and Stolz, 2005), whereas the low reaction rate in other
613 cases often leads to enhanced carbonates corrosion (e.g. Canfield & Raiswell, 1991). A number of studies
614 (e.g. Pinckney et al., 1995a,b; Abed et al., 2007) documented that rates of microbial processes are greatly
615 reduced under harsh hypersaline conditions, which is consistent for primary production, methanogenesis
616 and sulphate reduction. This supports the interpretation of the studied samples that a facies shift as well as
617 seasonal variation, through affecting the mat community, influenced the saturation state of the pore fluid
618 with respect to various carbonate minerals and, thus, the alteration processes of calcium-carbonate within
619 the mat deposits. Accordingly, the presence of large amounts of organic matter and evaporation in the
620 upper intertidal–lower supratidal zone under a semi-arid climate were the most important controlling
621 factors of both dolomite precipitation (DOL-1) and peritidal replacive dolomitization (DOL-2).
622 Infiltration of detrital dolomite silt into the pore system after the dissolution of the aragonite grains
623 implies high permeability and dynamic pore-fluid circulation. In Section 2, marine RFC cement
624 precipitation also indicates dynamic environmental conditions prior to the synsedimentary dolomitization.
625 Tidal pumping across the tidal flat is relatively short-lived but it is regarded as an efficient flow
626 mechanism for dolomitization of surficial intertidal sedimentary veneers (Carballo et al., 1987; Mazullo et
627 al., 1987; Gregg et al., 1992; Teal et al., 2000).
628
629 **8. Conclusions**
630
631 Petrographic analyses revealed a microbial origin for peritidal deposits of the Middle Triassic Budaörs
632 Dolomite. Initial organogenic precipitates within the microbial mat deposits included microcrystalline
633 dolomite as well as microcrystalline high-Mg calcite (HMC). Clusters of microcrystalline dolomite (DOL-
634 1) occur as calcimicrobes, clotted–spherular aggregates and globules in microbial boundstone whereas the
635 microcrystalline HMC was replaced by synsedimentary fine crystalline dolomite (DOL-2) and by
636 brownish-stained medium crystalline dolomite (DOL-3) in the bioclastic dolomite. In this latter case, the
637 fluorescence pattern revealed fenestral/desiccation pores and a clotted microfabric. The petrographic
638 features show that these two dolomite fabric types (FT1 and FT3) were formed under different
639 environmental conditions and consequently likely in different mat types, such as microbial boundstone in
640 the upper intertidal setting and bioclastic dolomite in the lower intertidal setting. Estimated oxygen isotope
641 values of synsedimentary dolomites (DOL-1 organogenic microcrystals and DOL-2 replacive fine
642 crystals) are consistent with dolomitization under mesohaline conditions, indicating a semi-arid climate.

643 All these data suggest that the diagenetic processes within peritidal deposits were likely controlled by
644 organic matter degradation together with environmental factors.
645 Synsedimentary dolomites were overprinted by a higher temperature (*ca* 65 to 80 °C) dolomitization in
646 intermediate burial depth that resulted in replacive and cement dolomite. This process was not restricted to
647 a particular depositional environment but affected the entire platform carbonate succession. An open half-
648 cell thermal convection system would explain the intermediate burial dolomitization.
649
650 **Acknowledgements**
651
652 We thank of Norbert Zajzon, Tamás Váczi and Zsolt Bendő for their assistance with geochemical
653 measurements, Olga Piros for the determination of fossils and Orsolya Győri for technical assistance. The
654 applied standards for the WDX measurements were courteously provided by the Department of Mineral
655 Sciences, Smithsonian National Museum of Natural History, Washington, USA. We are very grateful to
656 Henry Lieberman for grammatical corrections. Thorough review and valuable comments and suggestions
657 made by Brian R. Pratt and David A. Budd, which greatly improved the quality of the paper, are highly
658 appreciated. We are thankful to the two anonymous journal reviewers for comments and corrections. The
659 first author is a grantee of the Bolyai János Scholarship. Funding for this project was provided by the
660 Hungarian Scientific Research Fund, grant No. K 81296.
661
662 **References**
663
664 Abed, R.M.M., Kohls, K., De Beer, K., 2007. Effect of salinity changes on the bacterial diversity,
665 photosynthesis and oxygen consumption of cyanobacterial mats from an intertidal flat of the Arabian
666 Gulf. Environmental Microbiology 9/6, 1384–1392.
667 Abed, R.M.M., Kohls, K., Palinska, K.A., Golubic, S., 2010. Diversity and role of cyanobacteria and
668 aerobic heterotrophic microorganisms in carbon cycling in arid cyanobacterial mats. In*:* Seckbach, J.,
669 and Oren, A. (Eds), Microbial Mats, Modern and Ancient Microorganism in Stratified Systems.
670 Cellular Origin, Life in Extreme Habitats and Astrobiology Series 14, 255–276.
671 Allen, M.A., Goh, F., Burns, B.P., Neilan, B.A., 2009. Bacterial, archaeal and eukaryotic diversity of
672 smooth and pustular microbial mat communities in the hypersaline lagoon of Shark Bay. Geobiology
673 7, 82–96.
674 Banner, J.L., Hanson, G.N., 1990. Calculation of simultaneous isotopic and trace element variations
675 during water-rock interaction with applications to carbonate diagenesis. Geochemica et
676 Cosmochimica Acta 54, 3123–3137.

677 Baltzer, F., Kenig, F., Boichard, R., Plaziat, J.C., Purser, B.H., 1994. Organic matter distribution, water
678 circulation and dolomitisation beneath the Abu Dhabi Sabkha (UAE). In*:* Purser, B., Tucker, M.,
679 Zenger, D. (Eds), Dolomites. IAS Special Publication 21, 409–428.
680 Ben-Yaakov, S., 1973. pH buffering of pore water of recent anoxic marine sediments. Limnology and
681 Oceanography 18, 86–94.
682 Bertotti, G., Picotti, V., Bernoulli, D., Castellarin, A., 1993. From rifting to drifting: tectonic evolution of
683 the South-Alpine upper crust from the Triassic to the Early Cretaceous. Sedimentary Geology 86,
684 53–76.
685 Bertrand, P., Piton, J-L., Bernaud, C., 1986. Fluorescence of sedimentary organic matter in relation to its
686 chemical composition. Organic Geochemistry 10, 641–647.
687 Bontognali, T.R.R., Vasconcelos, C., Warthmann, R.J., Bernasconi, S.M., Dupraz, C., Strohmenger, C.J.,
688 McKenzie, J.A., 2010. Dolomite formation within microbial mats in the coastal sabkha of Abu
689 Dhabi (United Arab Emirates). Sedimentology 57, 824–844.
690 Braissant, O., Decho, A.W., Dupraz, C., Glunk, C., Przekop, K.M., Visscher, P.T., 2007. Exopolymeric
691 substances of sulfate-reducing bacteria: interactions with calcium at alkaline pH and implication for
692 formation of carbonate minerals. Geobiology 5, 401–411.
693 Budai, T., 2004. Middle Triassic basin facies and volcanites in the Zsámbék basin, Transdanubian Range,
694 Hungary. MÁFI Évi Jelentés 2002-ről 189–194 (in Hungarian with English summary).
695 Budd, D.A., 1997. Cenozoic dolomites of carbonate islands: their attributes and origin. Earth-Science
696 Review 42, 1–47.
697 Canfield, D.E., Raiswell, R., 1991. Carbonate precipitation and dissolution. Its relevance to fossil
698 preservation. In*:* Alison, P.A., Briggs, D.E.G. (Eds), Taphonomy. Releasing the Data Locked in the
699 Fossil Record. Plenum Press, New York, 411–453.
700 Carballo, J.D., Land, L.S., Miser, D.E., 1987. Holocene dolomitization of supratidal sediments by active
701 tidal pumping, Sugarloaf Key, Florida. Journal of Sedimentary Petrology 57, 153–165.
702 Choquette, P.W., Hiatt, E.E., 2008. Shallow-burial dolomite cement: a major component of many ancient
703 sucrosic dolomites. Sedimentology 55, 423–460.
704 Couradeau, E., Benzerara, K., Gérard, E., Estève, I., Moreira, D., Tavera, R., López-Garcia, P., 2013.
705 Cyanobacterial calcification in modern microbialites at the submicrometer scale. Biogeosciences
706 10, 5255–5266.
707 Csontos, L., Vörös, A., 2004. Mesozoic plate tectonic reconstruction of the Carpathian region.
708 Palaeogeography Palaeoclimatology Palaeoecology 210, 1–56.
709 Decho, A.W., Visscher, P.T., Reid, P., 2005. Production and cycling of natural microbial exopolymers
710 (EPS) within a marine stromatolite. Palaeogeography Palaeoclimatology Palaeoecology 219, 71–86.

711 Défarge, C., Trichet, J., Jaunet, A-M., Robert, M., Tribble, J., Sansone, F.J., 1996. Texture of microbial
712 sediments revealed by cryo-scanning electron microscopy. Journal of Sedimentary Research 66/5,
713 935–947.
714 Dickson, J.A.D., 1966. Carbonate identification and genesis as revealed by staining. Journal of
715 Sedimentary Petrology 36, 491–505.
716 Doglioni, C., 1992. Relationships between Mesozoic extensional tectonics, stratigraphy and Alpine
717 inversion in the Southern Alps. Eclogae Geologicae Helvetiae 85/1, 105–126.
718 Dravies, J.J., Yurewicz, D.A., 1985. Enhanced carbonate petrography using fluorescence microscopy.
719 Journal of Sedimentary Petrology 55, 795–804.
720 Dupraz, C., Vischer, P.T., Baumgartner, L.K., Reid, P., 2004. Microbe–mineral interactions: early
721 carbonate precipitation in a hypersaline lake (Eleuthera Island, Bahamas). Sedimentology 51, 745–
722 765.
723 Dupraz, C., Reid, P.R., Braissant, O., Decho, A., Norman, R.S., Visscher, P.T., 2009. Processes of
724 carbonate precipitation in modern microbial mats. Earth-Science Review 96, 141–162.
725 Fodor, L., Magyari, Á., Fogaras, A., Palotás, K., 1994. Tertiary tectonics and Late Paleogene
726 sedimentation in the Buda Hills, Hungary. A new interpretation of the Buda Line. Földtani Közlöny
727 124/2, 129–305.
728 Frank, T.D. and Lohmann, K.C., 1996. Diagenesis of fibrous magnesian calcite marine cement:
729 implications for the interpretation of δ18O and δ13C values of ancient equivalents. Geochimica et
730 Cosmochimica Acta 60/13, 2427–2436.
731 Gaft, M., Reisfeld, R., Panczer, G., 2005. Modern Luminescence Spectroscopy of Minerals and Materials.
732 Springer, Berlin Heidelberg.
733 Gallagher, K.L., Kading, T.J., Braissant, O., Dupraz, C., Visscher, P.T., 2012. Inside the alkalinity engine:
734 the role of electron donors in the organomineralization potential of sulphate-reducing bacteria.
735 Geobiology 10/6, 518–530.
736 Gautret, P., Camoin, G., Golubic, S., Sprachta, S., 2004. Biochemical Control of Calcium Carbonate
737 Precipitation in Modern Lagoonal Microbialites, Tikehau Atoll, French Polynesia. Journal of
738 Sedimentary Research 74/4, 462–478.
739 Goldstein, R.H., Reynolds, T.J., 1994. Systematics of Fluid Inclusions in Diagenetic Minerals. SEPM
740 Short Course 31.
741 Golubic, S., Abed, R.M.M., 2010. Entophysalis mats as environmental regulators. In*:* Seckbach, J., Oren,
742 A. (Eds), Microbial Mats, Modern and Ancient Microorganism in Stratified Systems Cellular
743 Orogin. Life in Extreme Habitats and Astrobiology Series 14, 239–254.

744 Gregg, J.M., Howard, S.A., Mazzulo, S.J., 1992. Early diagenetic recrystallization of Holocene (<3000
745 years old) peritidal dolomites, Ambergris Cay, Belize. Sedimentology 39, 143–160.
746 Győri, O., Poros, Zs., Mindszenty, A., Molnár, F., Fodor, L., Szabó, R., 2011. Diagenetic history of the
747 Palaeogene carbonates, Buda Hills, Hungary. Földtani Közlöny 141/4, 341–361 (in Hungarian with
748 English summary).
749 Haas, J., 2002. Origin and evolution of Late Triassic backplatform and intraplatform basins in the
750 Transdanubian Range, Hungary. Geologica Carpathica 53/3, 159–178.
751 Haas, J., Budai, T., 1995. Upper Permian-Triassic facies zones in the Transdanubian Range. Rivista
752 Italiana di Paleontologia e Stratigrafia 101/3, 249–266.
753 Haas, J., Budai, T., 1999. Triassic sequence stratigraphy of the Transdanubian Range, Hungary. Geologica
754 Carpathica 50/6, 459–475.
755 Haas, J. and Budai, T. 2004. Dunántúli –középhegységi egység. In: Haas, J. (Ed.), Magyarország
756 geológiája, triász, ELTE Eötvös Kiadó, Budapest, 25–124.
757 Halley, R.B., 1976. Textural variation within Great Salt Lake algal mounds. In*:* Walter, M.R. (Ed.),
758 Stromatolites. Elsevier, Amsterdam, 436–445.
759 Jahnert, R.J., Collins, L.B., 2013. Controls on microbial activity and tidal flat evolution in Shark Bay,
760 Western Australia. Sedimentology 60/4, 1071–1099.
761 Kandianis, M.T., Fouke, B.W., Johnson, R.W., Veysey II, J., Inskeep, W.P., 2007. Microbial biomass: A
762 catalyst for CaCO3 precipitation in advection-dominated transport regimes. Bulletin of Geological
763 Society of America 120/3–4, 442–450.
764 Kendall, A.C., 1985. Radiaxial-fibrous calcite: a reappraisal. In*:* Schneidermann, N., Harris, P.M. (Eds),
765 Carbonate Cements. SEPM Special Publication 36, 59–77.
766 Krause, S., Liebetrau, V., Gorb, S., Sánchez-Román, M., McKenzie, J.A., Treude, T., 2012. Microbial
767 nucleation of Mg-rich dolomite in exopolymeric substances under anoxic modern seawater salinity:
768 New insight into an old enigma. Geology 40, 587–590.
769 Krumbein, W.C., Garrels, R.M., 1952. Origin and classification of chemical sediments in terms of pH and
770 oxidation-reduction potentials. Journal of Geology 60/1, 1–33.
771 Kutassy, E., 1927. Beiträge zur Stratigraphie und Päleontologie der Alpinen Triasschichten in der
772 Umgebung von Budapest. Jahrbuch Königlichen Ungarischen Geologischen Anstalt 27/2, 105–175.
773 Land, L.S., 1983. The application of stable isotopes to studies of the origin of dolomite and to problems of
774 diagenesis of clastic sediments. In*:* Arthur, M.A., Anderson, T.F., Kaplan, I.R., Veizer, J., Land,
775 L.S. (Eds), Stable Isotopes in Sedimentary Geology. Society of Sedimentary Geology, Short Course
776 10, 4.1–4.22.
777 Land, L.S., 1985. The origin of massive dolomite. Journal of Geological Education 33, 112–125.

778 Land, L.S., Salem, M.R.I., Morrow, D.W., 1975. Paleohydrology of ancient dolomites: geochemical
779 evidence. AAPG Bulletin 59, 1602–1625.
780 Machel, H.G., 2004. Concepts and models of dolomitization: a critical reappraisal. In*:* Braithwaite, C.J.R.,
781 Rizzi, G., Darke, G. (Eds), The Geometry and Petrogenesis of Dolomite Hydrocarbon Reservoirs.
782 Geological Society of London, Special Publication 235, 7–63.
783 Magyari. Á., 1994. Late Eocene hydraulic rebrecciation in the Southern Buda Mountains, Hungary.
784 Földtani Közlöny 124/1, 89–107 (in Hungarian with English summary).
785 Magyari, Á., 1999. Törökugrató Hill: Late Eocene positive flower structure on the southwestern part of
786 the Buda Mountains, Budapest. Földtani Közlöny 128/4, 555–572 (in Hungarian with English
787 summary).
788 Márton, E., Fodor, L., 2003. Tertiary paleomagnetic results and structural analyses from the
789 Transdanubian Range (Hungary): rotational disintegration of the ALCAPA unit. Tectonophysics
790 363, 201–224.
791 Masetti, D., Neri, C., 1980. L'Anisico delia Val di Fassa (Dolomiti occidentali): sedimentologia e
792 paleografia. Annales University of Ferrara 7/1, 1–19.
793 Mastandrea, A., Perri, E., Russo, F., Spadafora, A., Tucker, M.E., 2006. Microbial primary dolomite from
794 a Norian carbonate platform, northern Calabria, southern Italy. Sedimentology 53, 465–480.
795 Mazullo, S.J., 2000. Organogenic dolomitization in peritidal to deep-sea sediments. Journal of
796 Sedimentary Research 70/1, 10–23.
797 Mazullo, S.J., Reid, A.M., Gregg, J.M., 1987. Dolomitization of Holocene Mg-calcite supratidal deposits,
798 Ambergris Cay, Belize. Geological Society of America Bulletin 98, 224–231.
799 McKenzie, J.A., 1981. Holocene dolomitization of calcium carbonate sediments from the coastal sabkhas
800 of Abu Dhabi, U.A.E.: A stable isotope study. Journal of Geology 89, 185–198.
801 Monty, C.L.V., 1976. The origin and development of cryptalgal fabrics. In*:* Walter, M.R., (Ed.),
802 Stromatolites. Elsevier, Amsterdam, 193–249.
803 Morrow, D.W., 1990. Dolomite – Part 2: Dolomitization models and ancient dolostones. In*:* McIlreath,
804 I.A., Morrow, D.W. (Eds), Diagenesis. Geoscience Canada, Reprint Series 4, 125–139.
805 Mutti, M., Simo, J.A. 1994. Distribution, petrography and geochemistry of early dolomite in cyclic shelf
806 facies, Yates Formation (Guadalupian), Capitanian Reef Complex, USA. In*:* Purser, B.H., Tucker,
807 M.E., Zenger, D.H. (Eds), Dolomites, a Volume in Honour of Dolomieu. IAS Special Publication
808 21, 91–107.
809 Paerl, H.W., Yannarell, A.C., 2010. Environmental dynamics, community structure and function in a
810 hypersaline microbial mat. In*:* Seckbach, J., Oren, A. (Eds), Microbial Mats, Modern and Ancient

811 Microorganism in Stratified Systems Cellular Origin. Life in Extreme Habitats and Astrobiology
812 Series 14, 423–444.
813 Perri, E., Tucker, M., 2007. Bacterial fossils and microbial dolomite in Triassic stromatolite. Geology
814 35/3, 207–210.
815 Pinckney, J., Paerl, H.W., Bebout, B.M., 1995a. Salinity control of benthic microbial mat community
816 production in a Bahamian hypersaline lagoon. Journal of Experimental Marine Biology and
817 Ecology 187, 223–237.
818 Pinckney, J., Paerl, H.W., Fitzpatrick, M., 1995b. Impacts of seasonality and nutrients on microbial mat
819 community structure and function. Marine Ecology Progress Series 123, 207–216.
820 Poros, Zs., 2011. Fluid migration and porosity evolution in the Buda Hills, Hungary – selected examples
821 from Triassic and Paleogene carbonate rocks. PhD dissertation, Eötvös University, Budapest.
822 Poros, Zs., Mindszenty A., Molnár, F., Pironon, J., Győri, O., Ronchi, P., Szekeres, Z., 2012. Imprints of
823 hydrocarbon-bearing basinal fluids on a karst system: mineralogical and fluid inclusion studies from
824 the Buda Hills, Hungary. International Journal of Earth Sciences 101, 429–452.
825 Pratt, B.R., 1984. *Epiphyton* and *Renalcis*—diagenetic microfossils from calcification of coccoid blue-
826 green algae. Journal of Sedimentary Petrology 54/3, 948–971.
827 Purser, B.H., Tucker, M.E., Zenger, D.H., 1994. Summary. In*:* Purser, B.H., Tucker, M.E., Zenger, D.H.
828 (Eds), Dolomites, a Volume in Honour of Dolomieu. IAS Special Publication 21, 29–33.
829 Read, J.F., Horbury, A.D., 1993. Eustatic and tectonic controls on porosity evolution beneath sequence-
830 bounding unconformities and parasequence disconformities on carbonate platforms. In*:* Horbury,
831 A.D., Robinson, A.G. (Eds), Diagenesis and Basin Development. AAPG Studies in Geology, Tulsa,
832 Oklahoma 36, 155–197.
833 Riding, R., 1991. Calcified Cyanobacteria. In*:* Riding, R. (Ed.), Calcareous Algae and Stomatolites.
834 Springer, Berlin, 55–87.
835 Riding, R., 2000. Microbial carbonates: the geological records of calcified bacterial–algal mats and
836 biofilms. Sedimentology 47/Suppl 1, 179–214.
837 Roberts, J.A., Kenward, P.A., Fowle, D.A., Goldstein, R.H., González, L.A., Moore, D.S., 2013. Surface
838 chemistry allows for abiotic precipitation of dolomite at low temperature. Proceedings of the national
839 Academy of Sciences of the USA 110/36, 14540–14545.
840 Rosenbaum, J., Sheppard, S.M.F., 1986. An isotopic study of siderites, dolomites and ankerites at high
841 temperatures. Geochemica et Cosmochimica Acta 50, 1147–1150.
842 Rüffer, T., Zühlke, R., 1995. Sequence stratigraphy and sea-level change in the Early to Middle Trassic of
843 the Alps: a global comparison. In*:* Haq, B.U. (Ed.), Sequence Stratigraphy and Depositional

844 Response to Eustatic, Tectonic and Climatic Forcing. Kluwer Academic Publishers, the Netherlands,
845 161–207.
846 Shinn, E., 1983. Tidal flat environment. In*:* Scholle, P.A., Bebout, D.G., Moore, C.H. (Eds), Carbonate
847 Depositional Environments. AAPG Memoir 33 171–210.
848 Simms, M.A., 1984. Dolomitization by groundwater flow systems in carbonate platforms. Transactions of
849 the Gulf Coast Association of Geological Sciences 24, 411–420.
850 Spadafora, A., Perri, E., McKenzie, J.A., Vasconcelos, C., 2010. Microbial biomineralization processes
851 forming modern Ca:Mg carbonate stromatolites. Sedimentology 57, 27–40.
852 Spötl, C., Vennemann, T.W., 2003. Continuous-flow isotope ratio mass spectrometric analysis of
853 carbonate minerals. Rapid Communication in Mass Spectrometry 17, 1004–1006.
854 Stephens, N.P., Sumner, D.Y., 2002. Renalcids as fossilized biofilm clusters. Palaios 17, 225–236.
855 Teal, C.S., Mazzulo, S.J., Bischoff, W.D., 2000. Dolomitization of Holocene shallow-marine deposits
856 mediated by sulphate reduction and methanogenesis in normal-salinity seawater, Northern Belize.
857 Journal of Sedimentary Research 70/3, 649–663.
858 Tucker, M.E., Wright, V.P., 1990. Carbonate Sedimentology. Blackwell Science, Oxford.
859 van Lith, Y., Warthmann, R., Vasconcelos, C, McKenzie, J.A., 2003. Sulphate-reducing bacteria induce
860 low-temperature Ca-dolomite and high Mg-calcite formation. Geobiology 1, 71–79.
861 Vasconcelos, C., McKenzie, J.A., Bernasconi, S., Grujic, D., Tiens, A.J., 1995. Microbial mediation as a
862 possible mechanism for natural dolomite formation at low temperatures. Nature 377, 220–222.
863 Visscher, P.Z., Stolz, J.F., 2005. Microbial mats as bioreactors: populations, processes, products.
864 Palaeogeography Palaeoclimatology Palaeoecology 219, 87–100.
865 Visscher, P.T., Reid, R.P., Bebout, B.M., 2000. Microscale observations of sulfate reduction: correlation
866 of microbial activity with lithified micritic laminae in modern marine stromatolites. Geology 28,
867 919–922.
868 Warren, J., 2000. Dolomite: occurrence, evolution and economically important associations. Earth-
869 Science Review 52, 1–81.
870 Wein, Gy., 1977. A Budai-hegység tektonikája (Tectonics of the Buda Hills). Hungarian Geological
871 Institute, Special Publication Budapest (in Hungarian).
872 Wenk, H.R., Hu, M., Frisia, S., 1993. Partially disordered dolomite: microstructural characterization of
873 Abu Dhabi sabkha carbonates. American Mineralogist 78/7–8, 769–774.
874 Whitaker, F.F., Xiao, Y., 2010. Reactive transport modelling of early burial dolomitization of carbonate
875 platforms by geothermal convection. AAPG Bulletin 94, 889–917.

876 Whitaker, F.F., Smart, P.L., Jones, G.D., 2004. Dolomitization: from conceptual to numerical models. In*:*
877 Braithwaite, C.J.R., Rizzi, G., Darke, G. (Eds), The Geometry and Petrogenesis of Dolomite
878 Hydrocarbon Reservoirs. Geological Society of London, Special Publication 235, 99–139.
879 Wilson, E.N., Hardie, L.A., Phillips, O.M., 1990. Dolomitization front geometry, fluid flow patterns, and
880 the origin of massive dolomite: the Triassic Latemar buildup, northern Italy. American Journal of
881 Science 290, 741–796.
882 Wilson, A.M., Sanford, W.E., Whitaker, F.F., Smart, P.L., 2001. Spatial patterns of diagenesis during
883 geothermal circulation in carbonate platforms. American Journal of Science 301, 727–752.
884 Wright, D.T., 1999. The role of sulphate-reducing bacteria and cyanobacteria in dolomite formation in
885 distal ephemeral lakes of the Coorong region, South Australia. Sedimentary Geology 126, 147–157.
886 Wright, D.T., Wacey, D., 2004. Sedimentary dolomite: a reality check. In*:* Braithwaite, C.J.R., Rizzi, G.,
887 Darke, G. (Eds), The Geometry and Petrogenesis of Dolomite Hydrocarbon Reservoirs. Geological
888 Society of London, Special Publication 235, 65–74.
889 Wright, D.T., Wacey, D., 2005. Precipitation of dolomite using sulfate-reducing bacteria from the
890 Coorong Region, South Australia: Significance and implication. Sedimentology 52, 987–1008.
891 Yannarell, A.C., Steppe, T.F., Paerl, H.W., 2006. Genetic variance in the composition of two functional
892 groups (diazotrophs and cyanobacteria) from a hypersaline microbial mat. Applied and
893 Environmental Microbiology 72/2, 1207–1217.
894 You, X., Sun, S., Zhu, J., Li, Q., Hu, W., Dong, H., 2013. Microbially mediated dolomite in Cambrian
895 stromatolites from the Tarim Basin, north-west China: implications for the role of organic substrate
896 on dolomite precipitation. Terra Nova 25/5, 387–395.
897

898 **Figure captions**

899 **Fig. 1. A**) Locations of the two studied sections (map by Haas, 2002). **B**) Pre-Quaternary geologic map of
900 the westernmost part of Buda Hills with the location of Section 1 (Fodor unpublished map 2000, modified
901 after Wein, 1977). Inset map showing Europe and Hungary with the location of map A. TransD.R.=
902 Transdanubian Range. Budapest and Budaörs are cities (grey).
903

904 **Fig. 2.** A–B) Panoramic view showing the position of the two studied sections and the logs of the sections.
905 C) A typical exposure of Section 1, showing the alternation of lithofacies. The thin-bedded/laminated
906 lithofacies (lower two-thirds) is overlain by the massive lithofacies (upper one-third).
907
908
909

910 **Fig. 3.** A typical micritic dolomite and microbial boundstone couplet of thin bedded/laminated lithofacies,
911 as exposed in Section 1, showing diagnostic features indicative of a peritidal environment (sample 4).
912
913 **Fig. 4.** Photomicrographs of microfabrics in the microbial boundstone. **A**) Framework structure,
914 composed of dense microcrystals (DOL-1), with bushy clot clusters (1). Dense micrite involves abundant
915 uniform, oval-shaped globules (scattered light dots, 2). The pore network is filled with coarser cement
916 crystals (lighter areas, 3). **B**) Higher magnification of densely-packed oval-shaped globules, interpreted as
917 ghosts of coccoid sheaths (red arrows). **C**) Clot clusters (1) and occluded various-sized
918 fenestral/desiccation pores (2). Brownish-coloured pendant cement (3) and pore-occluding fibrous cement
919 (4) are replaced by predominantly DOL-2 fine crystals and subordinately slightly brownish-coloured
920 DOL-3 medium-sized crystals. **D**) Fluorescence image of the field of view shown in C. DOL-1
921 microcrystals are bright green; the replaced pendant cement is dull green with growth zones; the fibrous
922 cement replaced by DOL-2 and DOL-3 exhibits very faint green mottles along growth bands in the non-
923 fluorescent groundmass. A–B: sample 6; C–D: sample 12.
924
925 **Fig. 5.** Photomicrographs of the microstructure and dolomite phases in the microbial boundstone. **A**) A
926 typical vertical pattern in the microstructure: the lower, thicker lamina is developed from the underlying
927 micritic dolomite (FT2) and gradually evolves into the upper lamina consisting of dense microcrystals
928 (DOL-1). The various-sized amalgamated nodules (1) are composed of microcrystalline aggregates (DOL-
929 1) and fine crystals (DOL-2). Large, quasi layer-parallel pores (2) and fractures (3) are occluded by DOL-
930 3 and DOL-4 phases. **B**) Distribution of crystal phases within the host deposits (dark grey areas on top and
931 bottom) and in a layer-parallel pore (middle). **C**) Fluorescence image of the field of view shown in C.
932 DOL-1 is bright green; DOL-2 is dull green; internal sediment 1is dull; CAL/DOL-3 has bright spots in a
933 non-fluorescent groundmass; DOL-4 has two growth bands that are dull with fine subzones and non-
934 fluorescent; internal sediment 2 is blotchy. A: sample 4; B–C: sample 6.
935
936 **Fig. 6.** Photomicrographs of the microbial boundstone showing the CL pattern of the crystal phases. **A**)
937 Nodular/reticulate lamina with DOL-1 microcrystals (white arrow), a mixture of DOL-1 microcrystals and
938 DOL-2 fine crystals (yellow arrow) and DOL-3 medium-sized crystals (red arrow). **B**) CL image of the
939 field of view shown in A. Dull red microcrystalline clotted groundmass (white arrow) involves nodules
940 exhibiting either less intense dull red luminescence (yellow arrow) or brighter spots in a non-luminescent
941 background (red arrow). **C**) Microbial boundstone (1) and pore-filling crystal phases, such as inclusion-
942 rich turbid DOL-3 coarse crystals (2) and limpid DOL-4 cement overgrowth (3). Surface of the DOL-4
943 crystals are serrated, corroded and occasionally covered by calcite microspars (4). Corrosion and calcite

944 precipitation was a result of recent meteoric alteration of the dolomite rocks. **D**) CL image of the field of
945 view shown in C. Crystal phases have specific CL patterns, such as: DOL-1 microcrystals are dull red (1),
946 DOL-3 crystals are mottled (2) and DOL-4 crystals have growth zones: non-luminescent and dull red (3).
947 Blotchy pattern characterises the corroded area of the DOL-4 crystals. Sample 4.
948
949 **Fig. 7.** Photomicrographs of the micritic dolomite. **A**) Tufted filamentous calcimicrobe (red arrow) and
950 microcrystalline lithoclasts with a sharp outline (yellow arrow) besides abundant DOL-2 fine crystals. **B**)
951 Fluorescence image of the field of view shown in A. Dull green groundmass of DOL-2 fine crystals
952 involves non-fluorescent and brighter mottles as well as bright green components consisting of DOL-1.
953 Pores (arrows) are filled by cement exhibiting two growth bands: mottled (scattered, brighter green dots in
954 a non-fluorescent background) and dull green–non-fluorescent. **C**) Mixture of crystal phases. Groundmass
955 of DOL-2 fine crystals (1) includes microcrystalline clot clusters (DOL-1; 2), microcrystalline lithoclasts
956 (DOL-1; 3) and DOL-3 medium-sized crystals (4). **D**) Fluorescence image of the field of view shown in
957 C. Bright microcrystalline clot clusters (top) have a gradual transition from the underlying dull green
958 finely crystalline spongy fabric. The fabric additionally consists of a few lithoclasts, having a sharp
959 boundary (yellow arrow), and pores are filled by mottled cement (red arrow). Sample 2.
960
961 **Fig. 8.** Photomicrographs of the bioclastic dolomite with ghosts of dasycladalean algae. **A**) Bands of
962 limpid crystals and/or dolomite silt fill biomoulds (yellow arrow). Brownish-coloured DOL-3 mosaic
963 crystals delineate the moulds (white arrow) and form patches (red arrow) in the finely crystalline
964 groundmass (DOL-2). **B**) Dolomite silt (DOL-2) and less inclusion-rich crystals (DOL-3 and DOL-4) fill
965 the biomoulds (yellow arrow), dark brown DOL-3 mosaic crystals delineate dasycladalean alga fragments
966 (white arrows) and dark brown DOL-3 mosaic crystals form patches (red arrow). Between them, brown
967 elongate crystals occur (blue arrow) which are surrounded by fine DOL-2 crystals. **C**) A dasycladalean
968 alga biomould and a primary intraparticle pore with dolomite phases. Dark brown DOL-3 mosaics cover
969 the bioclast surface both at the inner (white arrow, bottom left) and outer side (white arrow, top right);
970 lighter brown elongate DOL-3 crystals occur in the primary intraparticle pore (blue arrows); grey fine
971 DOL-2 crystals are dispersed among both types of DOL-3 crystals; the biomould pore is filled by
972 dolomite silt (yellow arrow on top) and less turbid DOL-3 and DOL-4 crystals (yellow arrows on left).—
973 Arrangement of brownish elongate crystals (RFC replaced by DOL-3) in the primary intraparticle pore
974 space indicates that they composed the first pore-filling cement phase. Fine crystals (DOL-2) partially
975 replaced the RFC and presumably the HMC crystals as well. **D**) Fluorescence image of the field of view
976 shown in C. Dark brownish-stained turbid DOL-3 mosaic crystals (which replaced the bioclast-covering
977 HMC) are bright green revealing the clot-clustered microfabric of the precursor carbonate (white arrows).

978 Micrite and elongate crystals (RFC replaced by DOL-2 and DOL-3, respectively) are mottled bright–dull
979 (blue arrows); cement in biomould has two growth bands: CAL replaced by turbid DOL-3 is mottled and
980 limpid DOL-4 overgrowth is non-fluorescent (yellow arrows on left); DOL-2 fine crystals, e.g. dolomite
981 silt (yellow arrow on top), are dull green. Sample 15.
982
983 **Fig. 9.** Photomicrograph of the transitional interval between the underlying bioclastic dolomite (FT3) and
984 the overlying microbial boundstone (FT1) where DOL-1 microcrystalline clot clusters appear in the fabric.
985 **A**) Microcrystalline DOL-1 (black) together with dark brown DOL-3 mosaic crystals (replaced HMC
986 precursor) form patches (red arrows) and cover the bioclasts (white arrows). Pore network is occluded by
987 crystal silt (DOL-2; grey) and/or two generations of cement (turbid CAL/DOL-3 and limpid DOL-4;
988 yellow arrow). **B**) Fluorescence image of the field of view shown in A. Both DOL-1 and dark brown
989 DOL-3 mosaic crystals show bright green fluorescence; DOL-2 fine crystals are dull green; and in the
990 pores, turbid DOL-3 crystals are mottled and limpid DOL-4 cement crystals are non-fluorescent. Sample
991 13.
992
993 **Fig. 10.** Photomicrographs of fabric-destructive dolomite in Section 1. **A**) Finely to medium crystalline
994 dolomite of massive lithofacies with lithoclast of microcrystalline to finely crystalline dolomite, having a
995 sharp outline (yellow arrow). Many reworked lithoclasts are typified by microcrystalline clot-clusters (red
996 arrow). **B**) Transitional interval (TR) between the underlying fabric-destructive dolomite and the overlying
997 microbial boundstone. In the fabric, DOL-1 microcrystalline clot clusters (black; white arrow) appear
998 among the DOL-2 fine (yellow arrow) and DOL-3 medium-sized (red arrow) crystals and thus, the
999 nodular/reticulate (NOD) microfabric becomes more obvious upwards. **C**) Fluorescence image of the field
1000 of view shown in B. The spongy fabric of precursor deposits is visible due to the different fluorescence of
1001 the components. A: sample 10; B–C: sample 1.
1002
1003 **Fig. 11.** Stable carbon and oxygen isotope data for whole rock fabrics (FT1, FT2, FT3 and FT4) and for
1004 pore-filling DOL-3, which replaced the CAL cement, and DOL-4 phases. Because of the small-scale
1005 heterogeneity of the studied rocks, the calculated mean values (larger dots) of the multiple analyses (small
1006 dots) of one sample are shown for the case where deviation of the oxygen isotope is larger than ±0.15‰.
1007
1008 **Fig. 12.** Fluid inclusion data from Section 1. **A**) An example of primary, two-phase (liquid–vapour)
1009 aqueous inclusion (arrow) hosted by the turbid DOL-3 phase which in turn replaced CAL cement; sample
1010 6). **B**) Homogenisation temperatures (Th) measured from DOL-3 and DOL-4 phases (samples 6 and 7).
1011

Fig. 13. Paragenetic sequence showing the successive diagenetic events that occurred up to the completion of dolomitization.

Fig. 14. Diagenetic alteration stages of the fabric of the studied cyclic deposits from deposition to intermediate burial realm up to the completion of dolomitization.

Table 1 Stable isotope values (V-PDB)

*Calculated mean values where deviation is larger than ±0.15‰.

Sample 3, fabric-destructive dolomite: –2.2 and –1.6‰.

Sample 9, pore-filling DOL-3 and DOL-4 phases: –2.6 and –2.0‰.

Sample 2, pore-filling DOL-3 and DOL-4 phases: –3.3 and –2.0‰.

Table 2 Fluid inclusion homogenisation temperature values

surface outcrops of Triassic formations

★ **Section 1:** N47°28.102 E18°56.909

★ **Section 2:** N47°32.583 E19°42.055

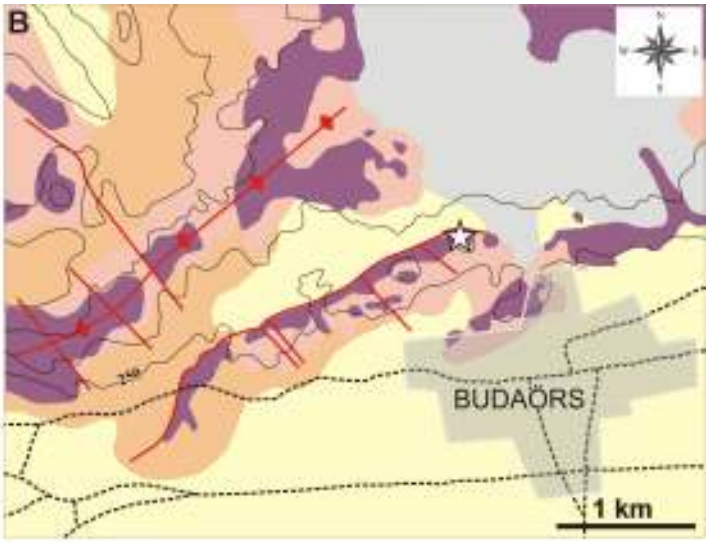

Miocene pebble, sand, freshwater limestone

Oligocene clay

Eocene–Oligocene marl

Eocene conglomerate

Triassic dolomite

faults

anticline structure

location of Section 1

roads

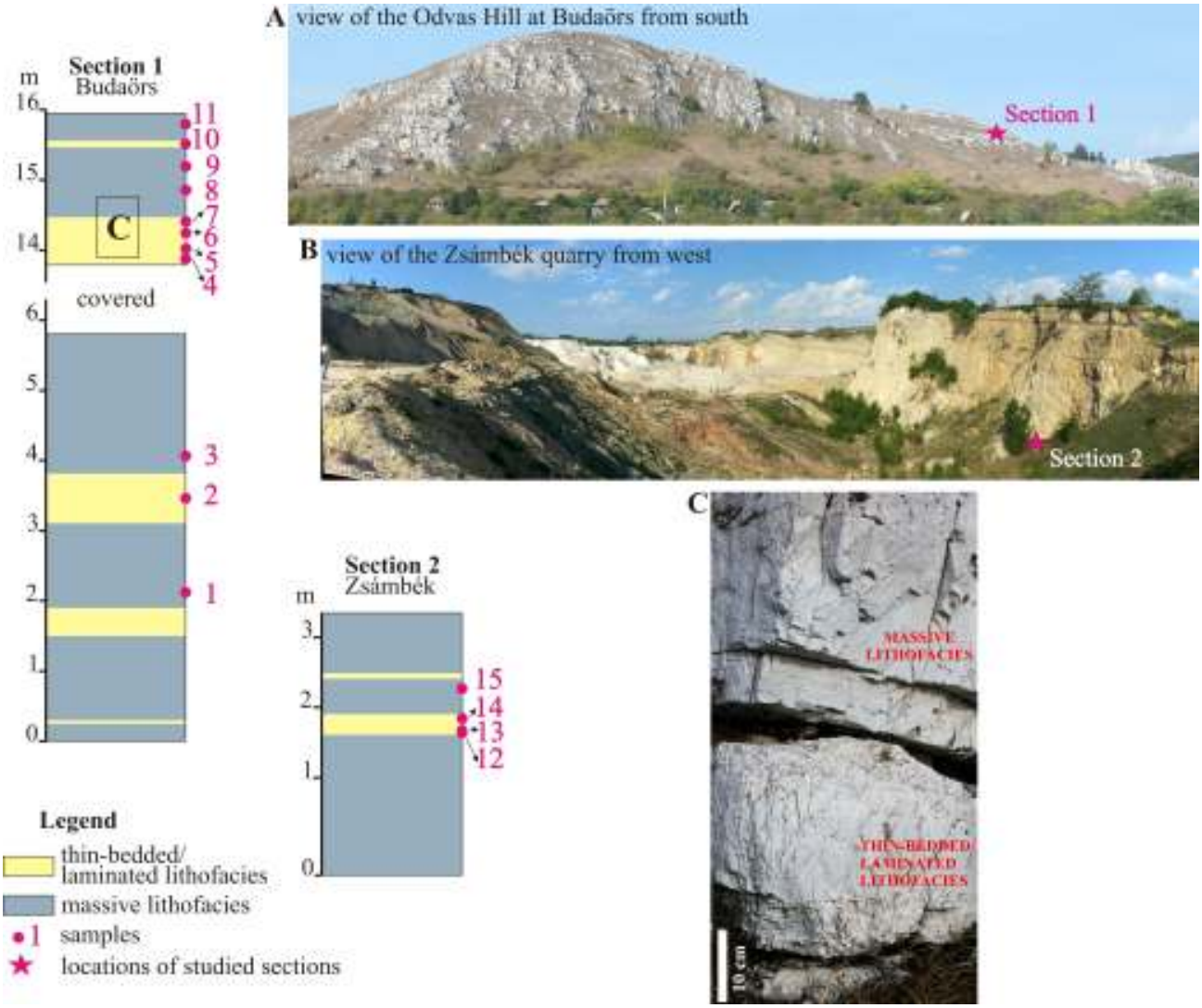
A view of the Odvas Hill at Budaörs from south
Section 1
B view of the Zsámbék quarry from west
Section 2
C
MASSIVE LITHOFACIES
THIN-BEDDED/ LAMINATED LITHOFACIES
10 cm
Section 1
Budaörs
m
16
15
14
C
11
10
9
8
7
6
5
4
covered
6
5
4
3
2
1
0
3
2
1
Section 2
Zsámbék
m
3
2
1
0
15
14
13
12
Legend
thin-bedded/ laminated lithofacies
massive lithofacies
1 samples
locations of studied sections

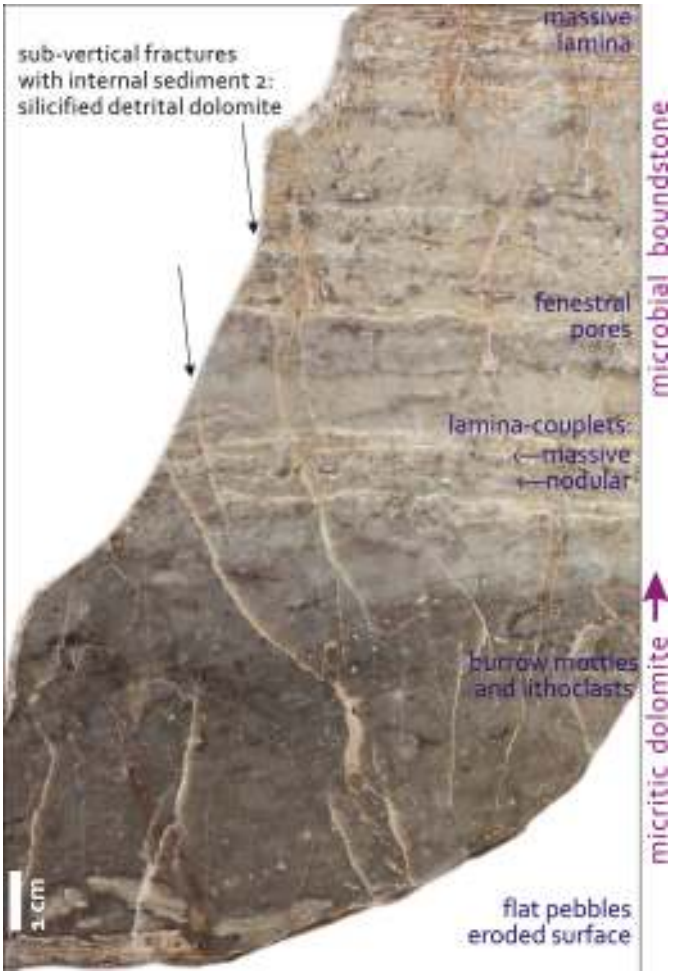
massive lamina
sub-vertical fractures with internal sediment 2: silicified detrital dolomite
fenestral pores
lamina-couplets:
massive
nodular
burrow mottles and lithoclasts
1 cm
flat pebbles eroded surface
microbial boundstone
micritic dolomite

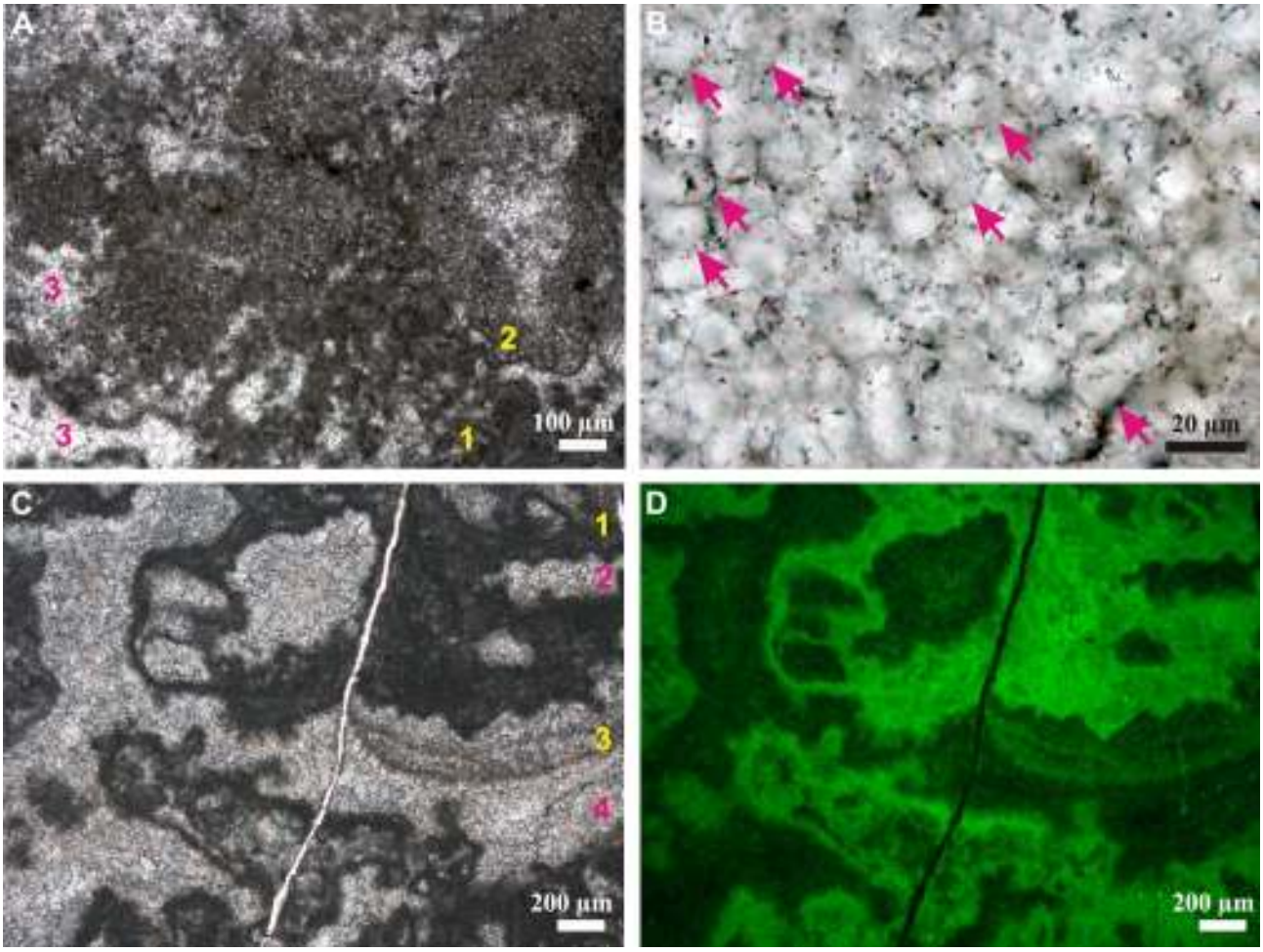
A
3
2
3
1
100 µm
B
20 µm
C
1
2
3
4
200 µm
D
200 µm

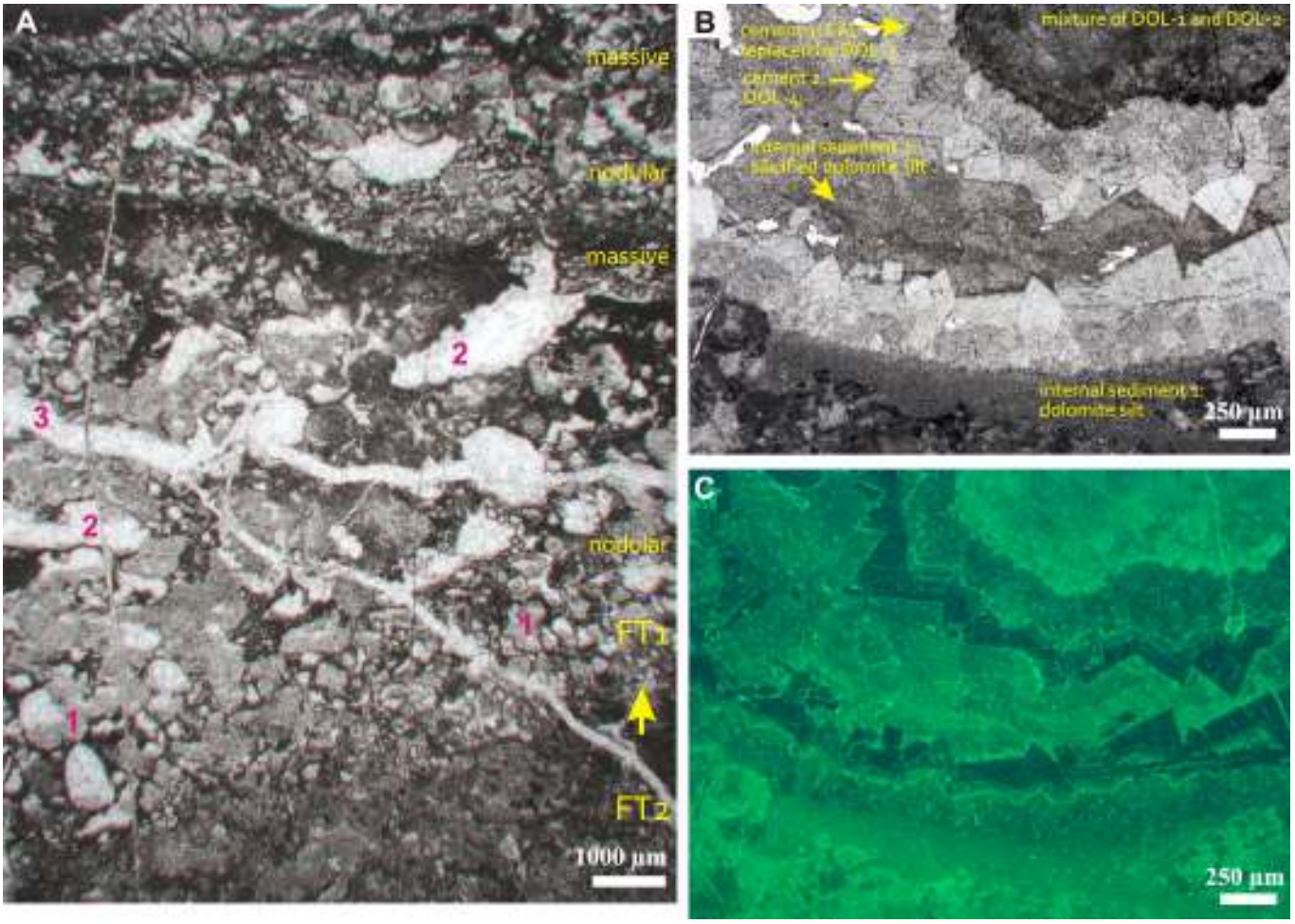
A
massive
nodular
massive
2
3
2
nodular
1
FT1
1
FT2
1000 µm
B
mixture of DOL-1 and DOL-2
cement-2:
DOL-2
internal sediment 2:
dolomite silt
250 µm
C
250 µm

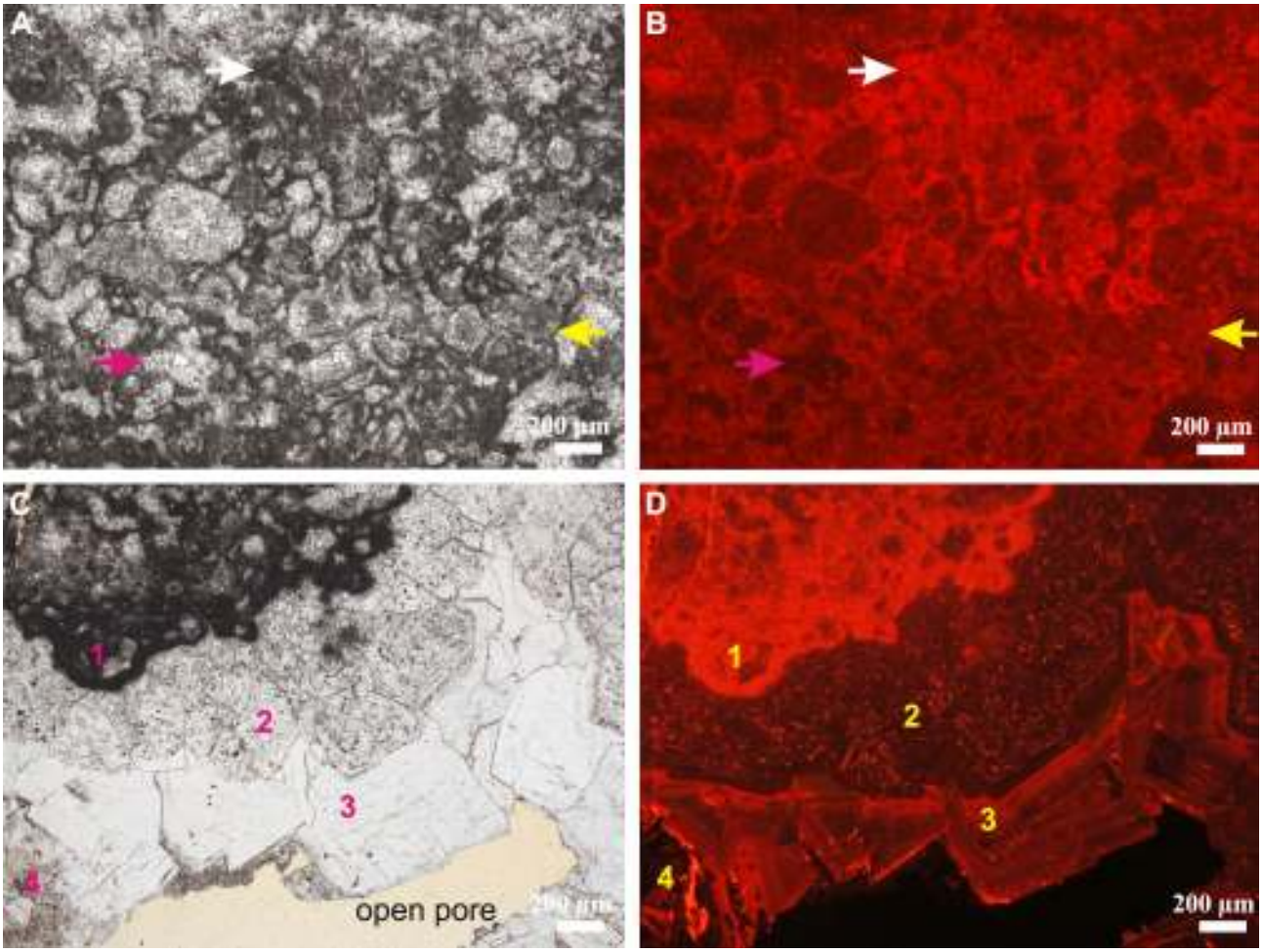
A
200 µm
B
200 µm
C
1
2
3
4
open pore
D
1
2
3
4
200 µm

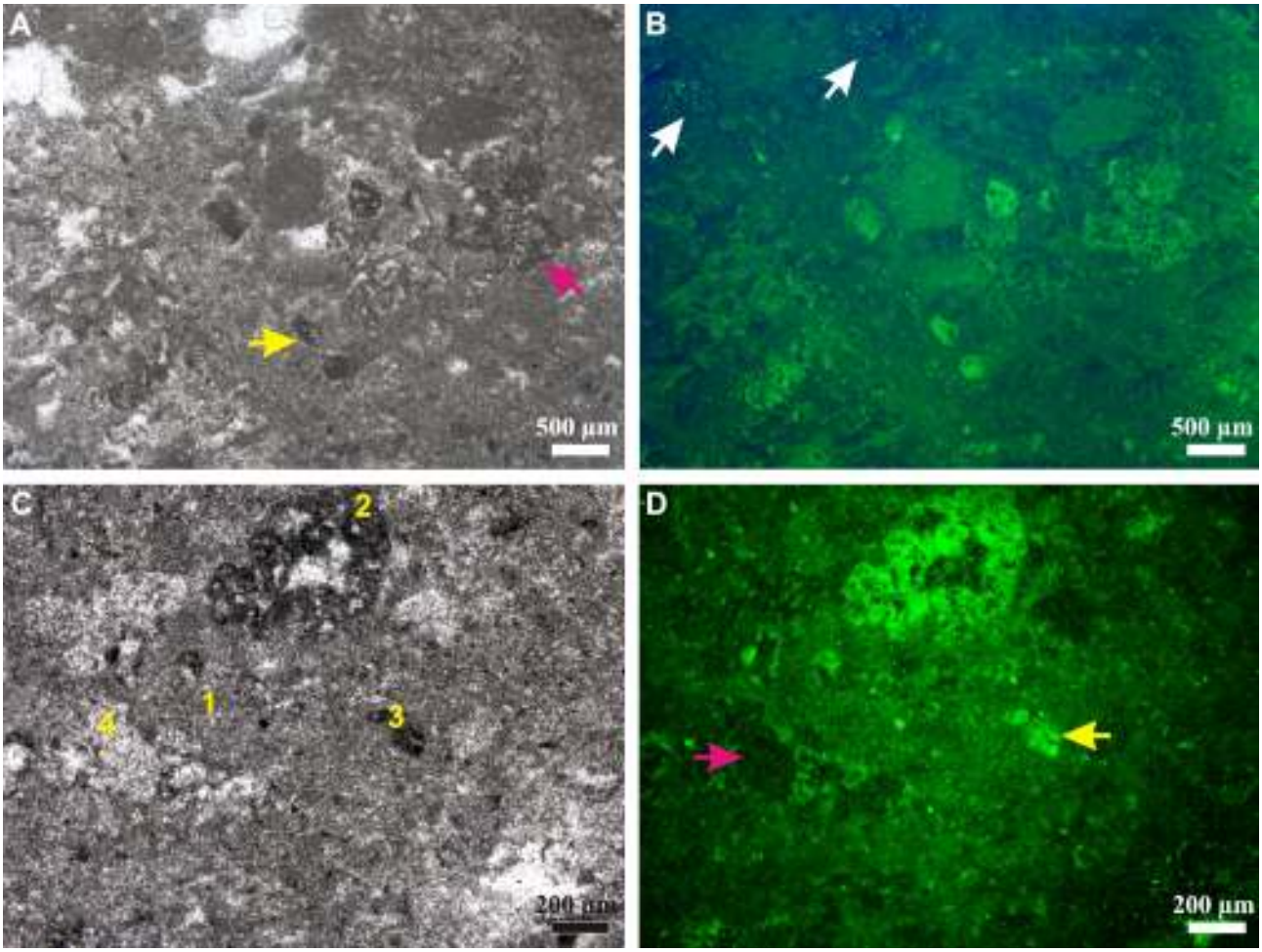
A
500 μm
B
500 μm
C
2
1
3
4
200 μm
D
200 μm

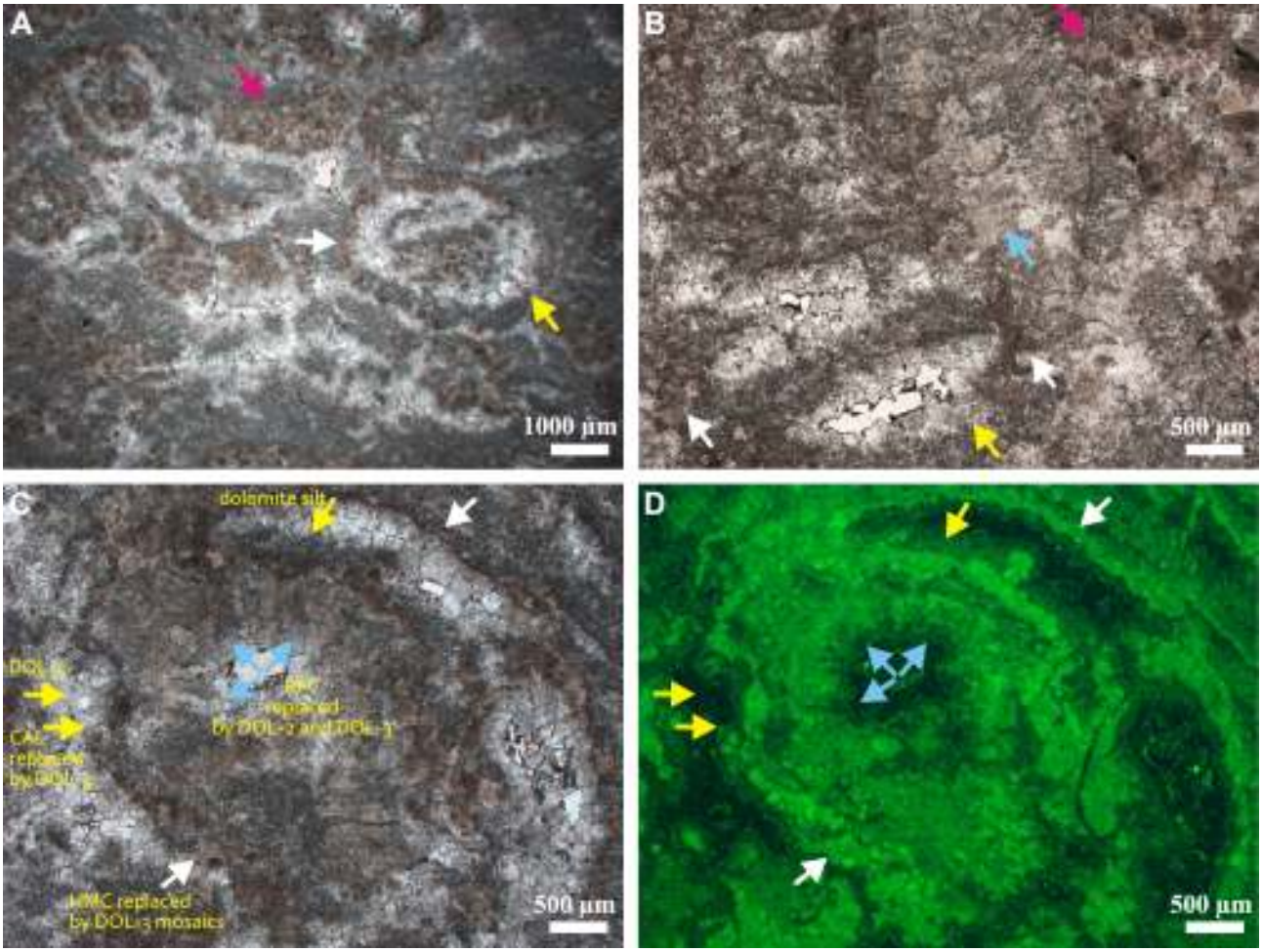
A
1000 μm
B
500 μm
C
dolomite silt
500 μm
D
500 μm

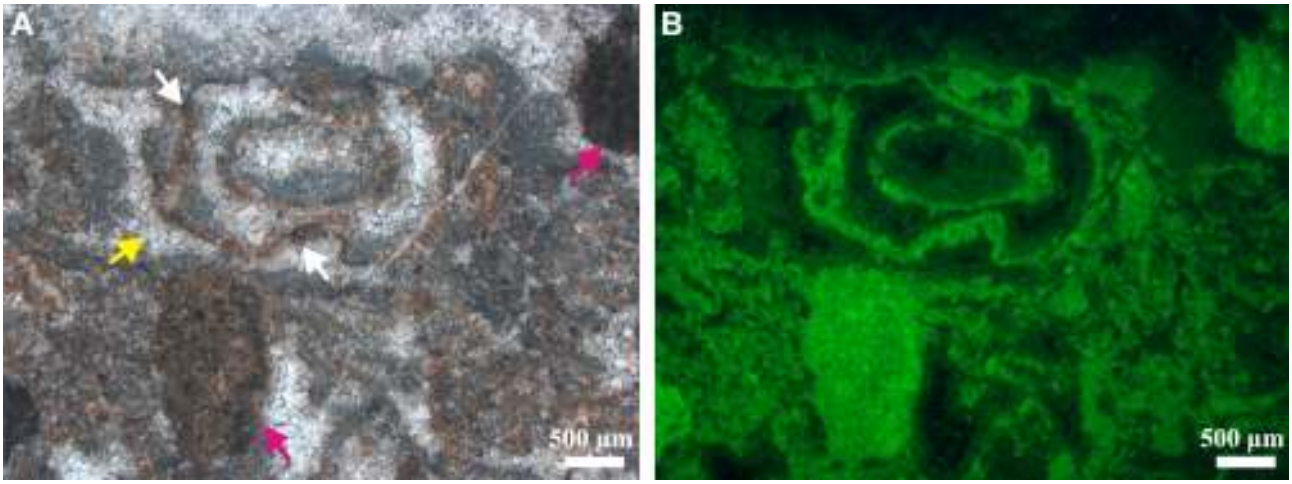
A
500 µm
B
500 µm

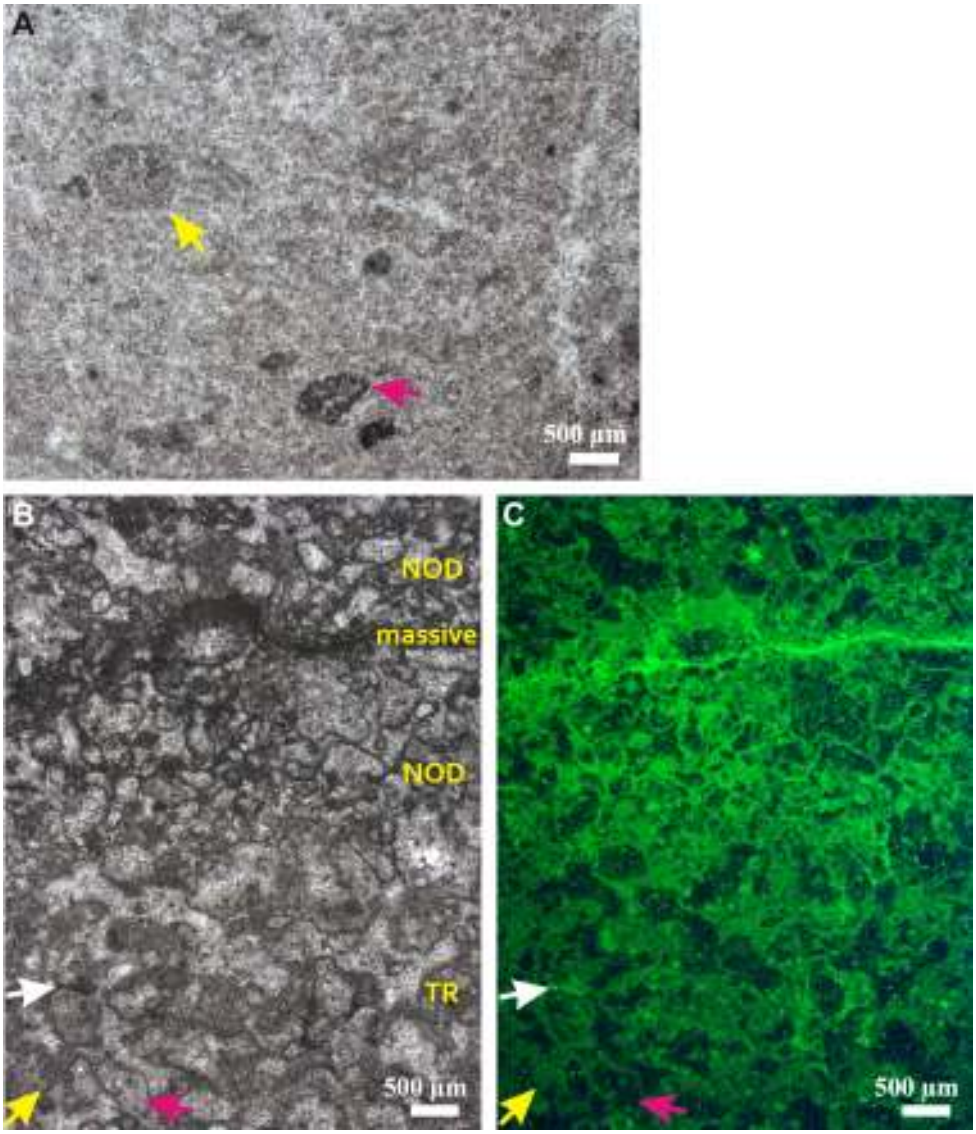
A
500 µm
B
NOD
massive
NOD
TR
500 µm
C
500 µm

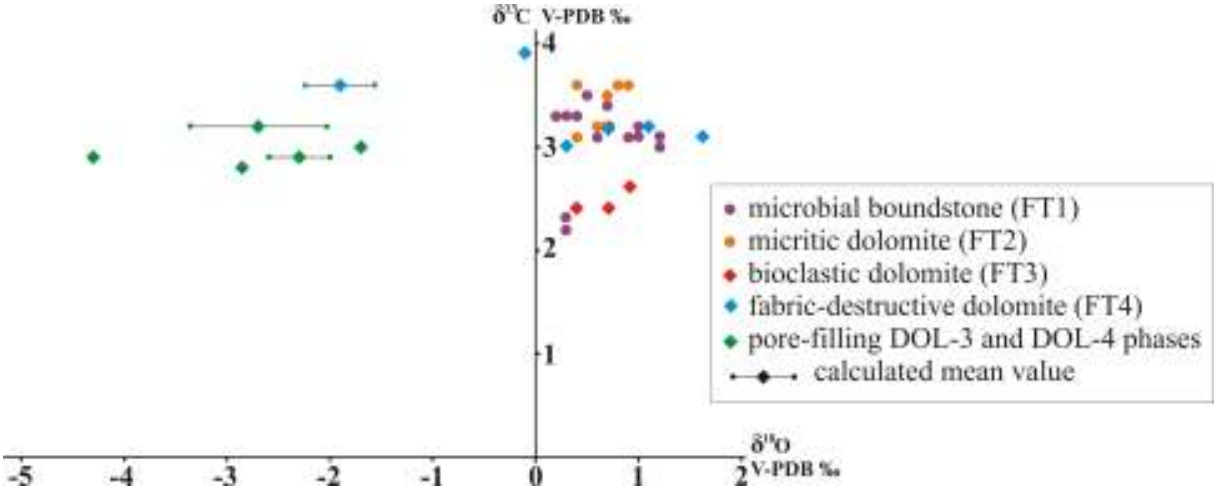
δ13C V-PDB ‰
4
3
2
1
-5
-4
-3
-2
-1
0
1
2
δ18O V-PDB ‰
microbial boundstone (FT1)
micritic dolomite (FT2)
bioclastic dolomite (FT3)
fabric-destructive dolomite (FT4)
pore-filling DOL-3 and DOL-4 phases
calculated mean value


A
10 μm

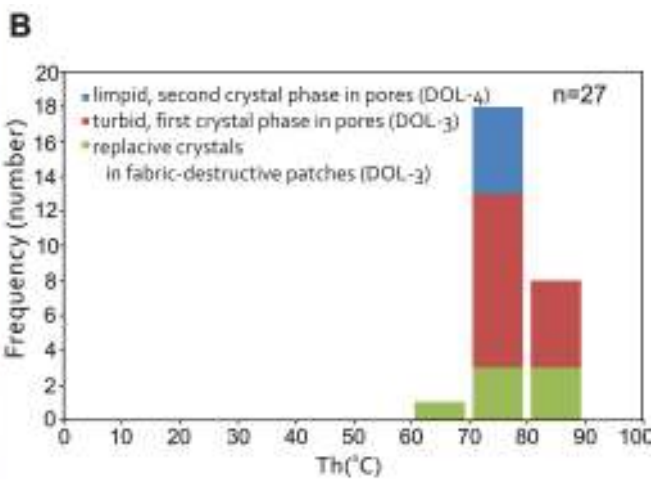
B
limpid, second crystal phase in pores (DOL-4)
turbid, first crystal phase in pores (DOL-3)
replacive crystals
in fabric-destructive patches (DOL-3)
n=27
Frequency (number)
Th(°C)
0
2
4
6
8
10
12
14
16
18
20
0
10
20
30
40
50
60
70
80
90
100

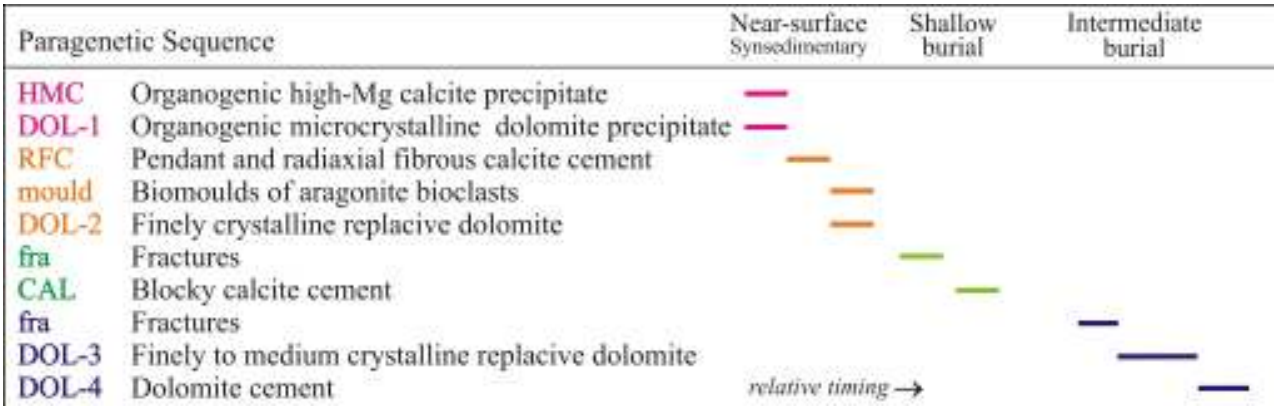
Paragenetic Sequence
Near-surface
Synsedimentary
Shallow
burial
Intermediate
burial
HMC
Organogenic high-Mg calcite precipitate
DOL-1
Organogenic microcrystalline dolomite precipitate
RFC
Pendant and radiaxial fibrous calcite cement
mould
Biomoulds of aragonite bioclasts
DOL-2
Finely crystalline replacive dolomite
fra
Fractures
CAL
Blocky calcite cement
fra
Fractures
DOL-3
Finely to medium crystalline replacive dolomite
DOL-4
Dolomite cement
relative timing →

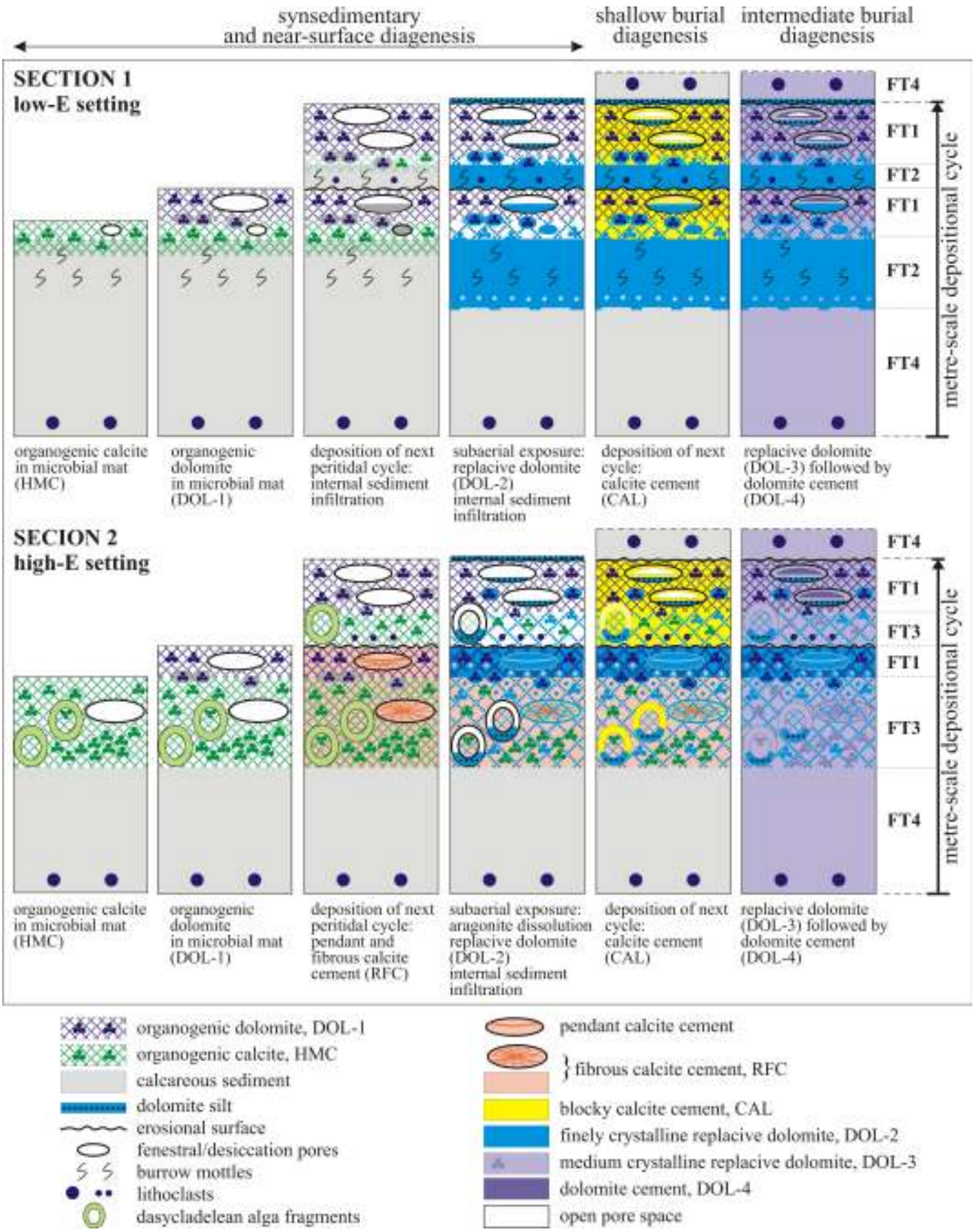
synsedimentary
and near-surface diagenesis
shallow burial
diagenesis
intermediate burial
diagenesis
SECTION 1
low-E setting
FT4
FT1
FT2
FT1
FT2
FT4
metre-scale depositional cycle
organogenic calcite in microbial mat (HMC)
organogenic dolomite in microbial mat (DOL-1)
deposition of next peritidal cycle: internal sediment infiltration
subaerial exposure: replacive dolomite (DOL-2) internal sediment infiltration
deposition of next cycle: calcite cement (CAL)
replacive dolomite (DOL-3) followed by dolomite cement (DOL-4)
SECION 2
high-E setting
FT4
FT1
FT3
FT1
FT3
FT4
metre-scale depositional cycle
organogenic calcite in microbial mat (HMC)
organogenic dolomite in microbial mat (DOL-1)
deposition of next peritidal cycle: pendant and fibrous calcite cement (RFC)
subaerial exposure: aragonite dissolution replacive dolomite (DOL-2) internal sediment infiltration
deposition of next cycle: calcite cement (CAL)
replacive dolomite (DOL-3) followed by dolomite cement (DOL-4)
organogenic dolomite, DOL-1
organogenic calcite, HMC
calcareous sediment
dolomite silt
erosional surface
fenestral/desiccation pores
burrow mottles
lithoclasts
dasycladelean alga fragments
pendant calcite cement
fibrous calcite cement, RFC
blocky calcite cement, CAL
finely crystalline replacive dolomite, DOL-2
medium crystalline replacive dolomite, DOL-3
dolomite cement, DOL-4
open pore space

Sample	Dolomite fabric	$\delta^{13}C$ (‰)	$\delta^{18}O$ (‰)
4	microbial boundstone	3.1	1.2
1	microbial boundstone	3.0	1.2
1	microbial boundstone	3.1	1.0
4	microbial boundstone	3.2	1.0
4	microbial boundstone	3.2	1.0
4	microbial boundstone	3.1	0.9
2	microbial boundstone	3.4	0.7
6	microbial boundstone	3.2	0.7
4	microbial boundstone	3.1	0.6
2	microbial boundstone	3.5	0.5
2	microbial boundstone	3.3	0.4
2	microbial boundstone	3.3	0.3
12	microbial boundstone	2.2	0.3
12	microbial boundstone	2.3	0.3
2	microbial boundstone	3.3	0.2
2	micritic dolomite	3.6	0.9
2	micritic dolomite	3.6	0.8
2	micritic dolomite	3.5	0.7
4	micritic dolomite	3.2	0.7
4	micritic dolomite	3.2	0.6
2	micritic dolomite	3.6	0.4
4	micritic dolomite	3.1	0.4
15	bioclastic dolomite	2.6	0.9
15	bioclastic dolomite	2.4	0.7
15	bioclastic dolomite	2.4	0.4
1	fabric-destructive dolomite	3.1	1.6
1	fabric-destructive dolomite	3.1	1.6
1	fabric-destructive dolomite	3.2	1.1
1	fabric-destructive dolomite	3.2	0.7
10	fabric-destructive dolomite with lithoclasts	3.0	0.3
3	fabric-destructive dolomite	3.9	-0.1
3	fabric-destructive dolomite	3.6	-1.9*
4	pore-filling DOL-3 and DOL-4 phases	3.0	-1.7
9	pore-filling DOL-3 and DOL-4 phases	2.9	-2.3*
2	pore-filling DOL-3 and DOL-4 phases	3.2	-2.7*
10	pore-filling DOL-3 and DOL-4 phases	2.8	-2.8
8	pore-filling DOL-3 and DOL-4 phases	2.9	-4.3

Sample	Dolomite fabric	Th (ºC)
6	turbid crystal phase in pores, DOL-3	81.7
6	turbid crystal phase in pores, DOL-3	75
6	turbid crystal phase in pores, DOL-3	79
6	turbid crystal phase in pores, DOL-3	82
6	turbid crystal phase in pores, DOL-3	85
6	turbid crystal phase in pores, DOL-3	77
6	turbid crystal phase in pores, DOL-3	87
6	limpid crystal phase in pores, DOL-4	75
7	turbid crystal phase in pores, DOL-3	74
7	turbid crystal phase in pores, DOL-3	73
7	turbid crystal phase in pores, DOL-3	73.8
7	turbid crystal phase in pores, DOL-3	73
7	turbid crystal phase in pores, DOL-3	78
7	turbid crystal phase in pores, DOL-3	90
7	turbid crystal phase in pores, DOL-3	79
7	turbid crystal phase in pores, DOL-3	72
7	replacive crystal in fabric-destructive patches, DOL-3	74
7	replacive crystal in fabric-destructive patches, DOL-3	83
7	replacive crystal in fabric-destructive patches, DOL-3	62
7	replacive crystal in fabric-destructive patches, DOL-3	80
7	replacive crystal in fabric-destructive patches, DOL-3	78
7	replacive crystal in fabric-destructive patches, DOL-3	82
7	replacive crystal in fabric-destructive patches, DOL-3	82
7	limpid crystal phase in pores, DOL-4	75
7	limpid crystal phase in pores, DOL-4	79
7	limpid crystal phase in pores, DOL-4	79
7	limpid crystal phase in pores, DOL-4	78